Jupiter's low-altitude auroral zones: Fields, particles, plasma waves, and density depletions

A. H. Sulaiman,[1] F. Allegrini,[2,3] G. Clark,[4] G. R. Gladstone,[2,3] S. Kotsiaros,[5] W. S. Kurth,[1] B. H. Mauk,[4] J. R. Szalay,[6] F. Bagenal,[7] B. Bonfond,[8] J. E. P. Connerney,[9,10] R. W. Ebert,[2,3] S. S. Elliott,[11] D. J. Gershman,[10] G. B. Hospodarsky,[1] V. Hue,[2] R. L. Lysak,[11] A. Masters,[12] O. Santolík,[13,14] J. Saur,[15] S. J. Bolton[1]

Corresponding author: A.H. Sulaiman, Department of Physics and Astronomy, University of Iowa, Iowa City, Iowa, USA. (ali-sulaiman@uiowa.edu)

[1]Department of Physics and Astronomy, University of Iowa, Iowa City, IA, USA.

[2]Southwest Research Institute, San Antonio, TX, USA.

[3]Department of Physics and Astronomy, University of Texas at San Antonio, San Antonio, TX, USA.

[4]Johns Hopkins University, Applied Physics Laboratory, Laurel, MD, USA.

[5]DTU-Space, Technical University of Denmark, Kongens Lyngby, Denmark

[6]Department of Astrophysical Sciences, Princeton University, Princeton, NJ, USA

[7]Laboratory for Atmospheric and Space Physics, University of Colorado Boulder, Boulder, CO, USA.

[8]Space Sciences, Technologies and Astrophysics Research Institute, LPAP, Université de Liège, Liège, Belgium

[9]Space Research Corporation, Annapolis, MD, USA

[10]NASA/Goddard Space Flight Center, Greenbelt, Maryland, USA.

[11]Minnetota Institute for Astrophysics, School of Physics and Astronomy, University of Minnesota, Minneapolis, MN, USA.

[12]Blackett Laboratory, Imperial College London, London, UK.

[13]Department of Space Physics, Institute of Atmospheric Physics of the Czech Academy of Sciences, Prague, Czechia.

[14]Faculty of Mathematics and Physics, Charles University, Prague, Czechia.

[15]Institute of Geophysics and Meteorology, University of Cologne, Cologne, Germany

- We discuss how the various fields, particles, and plasma wave phenomena of Jupiter's low-altitude auroral zones are related
- We confirm that Zone-I and Zone-II are Jupiter's upward and downward field-aligned current regions
- We identify large-scale electron density depletions over the aurora zones and discuss the implications for auroral acceleration processes

Abstract

The Juno spacecraft's polar orbits have enabled direct sampling of Jupiter's low-altitude auroral field lines. While various datasets have identified unique features over Jupiter's main aurora, they are yet to be analyzed altogether to determine how they can be reconciled and fit into the bigger picture of Jupiter's auroral generation mechanisms. Jupiter's main aurora has been classified into distinct "zones", based on repeatable signatures found in energetic electron and proton spectra. We combine fields, particles, and plasma wave datasets to analyze Zone-I and Zone-II, which are suggested to carry the upward and downward field-aligned currents, respectively. We find Zone-I to have well-defined boundaries across all datasets. H^+ and/or H_3^+ cyclotron waves are commonly observed in Zone-I in the presence of energetic upward H^+ beams and downward energetic electron beams. Zone-II, on the other hand, does not have a clear poleward boundary with the polar cap, and its signatures are more sporadic. Large-amplitude solitary waves, which are reminiscent of those ubiquitous in Earth's downward current region, are a key feature of Zone-II. Alfvénic fluctuations are most prominent in the diffuse aurora and are repeatedly found to diminish in Zone-I and Zone-II, likely due to dissipation, at higher altitudes, to energize auroral electrons. Finally, we identify sharp and well-defined electron density depletions, by up to two orders of magnitude, in Zone-I, and discuss their important implications for the development of parallel potentials, Alfvénic dissipation, and radio wave generation.

1. Introduction

The combination of Jupiter's strong magnetic field, rapid rotation, and internally sourced mass loading creates a magnetosphere that is fundamentally different from its terrestrial counterpart. Structurally, the magnetosphere is inflated with the average observed distance of the magnetopause far greater than the expected distance predicted from the internal dipolar magnetic pressure standing off the external solar wind dynamic pressure (Joy et al. 2002). Mass loading of iogenic plasma in the magnetosphere at a widely assumed rate of ~1 ton/s, primarily in the form of S and O (in various charge states), greatly enhances the internal pressure owing to centrifugal, thermal, and magnetic stresses, thereby pushing the magnetopause farther out. The action of these forces confines the heavy plasma into the equatorial region of Jupiter's magnetosphere as a thin current sheet, with varying thickness as a function of local time imposed by Jupiter's rotation (Khurana et al., 2004; Thomas et al., 2004).

Dynamically, conservation of angular momentum breaks down the corotation of iogenic plasma as it is transported radially outward. This introduces a significant azimuthal component to Jupiter's magnetic field, starting in the middle magnetosphere ($\gtrsim$ 10 R_J; 1 R_J = 71,492 km as Jupiter's equatorial radius). This large-scale configuration has been thought to be the framework for Jupiter's main auroral oval as a current system imparts the required $\mathbf{J} \times \mathbf{B}$ force to enforce corotation (Hill, 1979; Cowley & Bunce, 2001; Kivelson & Southwood, 2005). Charge density continuity is satisfied by field-aligned currents and this is the basis upon which magnetosphere-ionosphere coupling is established. This steady-state picture has been modelled extensively to explain the observed brightness and location of Jupiter's main auroral oval (e.g. Nichols and Cowley, 2004; Ray et al., 2010) by citing a relationship between parallel potentials and field-aligned currents, originally developed for Earth's aurora (Knight, 1973). A consequence of this is a mono-energetic or peaked electron distribution as current-carrying electrons unidirectionally gain energy, $q\phi_{||}$, proportional to the potential drop. A different approach put forth by Saur et al. (2002, 2003) emphasizes the importance of prevalent small-scale magnetic perturbations brought about by radial transport in Jupiter's magnetosphere. The authors hypothesized that Jupiter's magnetosphere-ionosphere coupling is inherently time-dependent and mediated by weak magnetohydrodynamic turbulence, whereby Alfvén waves nonlinearly interact with one another as they partially reflect off density gradients. As these fluctuations undergo a turbulent cascade toward kinetic scales, wave dissipation takes place and stochastically accelerates electrons. The commonly observed broadband, bidirectional electron distributions in the low altitude regions of Jupiter's aurora have brought to the fore the importance of the time-dependent nature of Jupiter's magnetosphere (e.g, Mauk et al., 2017a; 2017b; Allegrini et al., 2017; Saur et al., 2018; Lysak et al., 2021).

Prior to Juno's arrival, Jupiter's main aurora was investigated using remote observations and was found to be more powerful and less variable than Earth's aurora (e.g. Waite et al., 2001; Gladstone et al., 2002; Grodent et al., 2015). The principal difference is that Jupiter's aurora is primarily driven by the internal dynamics of its magnetosphere, whereas Earth's is primarily driven by the external solar wind (Cowley & Bunce, 2001; Hill, 2001). Recent modelling shows that most of the polar cap region is threaded by magnetic flux that closes within the planet while only a small crescent-shaped region of flux is 'open' to the solar wind (Zhang et al., 2021). This is attributed to slow reconnection rates at the magnetopause relative to the timescale of planetary rotation, thereby

limiting the amount of magnetic flux that can be open (McComas and Bagenal, 2007; Delamere and Bagenal, 2010; Masters, 2017; 2018).

The Juno spacecraft's low-perijove, polar orbits have enabled *in-situ* sampling of low-altitude magnetic field lines threading Jupiter's polar aurora (e.g., Allegrini et al., 2017; Kurth et al., 2017a; Mauk et al., 2017c). Juno's instruments have made direct measurements of critical observables connected to the main aurora, namely the characteristics of precipitating electrons (e.g., Allergini et al., 2020a; Mauk et al., 2020), magnetic field perturbations (Kotsiaros et al., 2019; Gershman et al., 2019), radio and plasma wave emissions (e.g., Kurth et al., 2017a; 2018; Louarn et al., 2017), as well as high-resolution ultraviolet (e.g., Bonfond et al., 2017; Gladstone et al., 2017) and infrared (e.g., Mura et al., 2017) imagery. Altogether, these afford the capability to examine the seemingly unique macro- and micro-physics sustaining Jupiter's aurora.

A key finding related to Jupiter's auroral particles is the often-observed broadband energetic field-aligned electrons with a power law extending into the MeV range and a lack of sharp peak in energy (Mauk et al., 2017a; 2017b; 2018). These electron beams can have energy fluxes exceeding 3 W/m^2 and exhibit bidirectionality that is more often asymmetric, with a systematically preferred direction depending on latitude (Mauk et al., 2020). This appears to be the dominant precipitating electron signature associated with the brightest aurora at Jupiter (Allegrini et al., 2020a; Mauk et al., 2017b) and is in contrast with Earth's brightest aurora where they have been demonstrated to be powered by inverted V distributions set up by parallel potentials (Carlson et al., 1998; Ergun et al., 1998). The more familiar peaked energy distributions in the form of inverted-V electron and ion distributions have also been observed by Juno, indicating that large-scale parallel electric potentials also play a role (Clark et al., 2017; 2018). Although these two phenomena are disparate in nature, they are believed to be closely associated with one another and have both been identified to operate together in a single auroral zone as defined by Mauk et al. (2020) and summarized below.

Using the JEDI instrument (described in the next section) with orbits favoring the duskside, Mauk et al. (2020) classified Jupiter's main aurora into three distinct zones, two of which will be the focus of this work. These are Zone-I and Zone-II, comprising regions of the aurora dominated by persistent and repeatable signatures of field-aligned energetic electrons.

1. Zone-I (ZI): At the intermediate latitudes of the main auroral oval, this is characterized by more intense electron populations within the downward loss cone than outside, and with greater downward electron intensities and energy fluxes than upward.
2. Zone-II (ZII): At the higher latitudes, this is characterized by more intense electron populations within the upward loss cone than outside, and with greater or equal upward electron intensities and energy fluxes than downward. Here, remarkably, the downward fluxes are nevertheless still sufficient to cause observable and powerful auroral intensities.

Zone-I and Zone-II have been suggested to be associated with upward and downward electric currents, respectively, for a single event (Mauk et al., 2020). Equatorward of these zones is the diffuse aurora (Dif-A), characterized with more intense high-energy electron populations outside of the loss cone than within, and with greater downward electron intensities and energy fluxes than upward.

Poleward of the zones is the polar cap – a vast and dynamic region where persistent highly field-aligned, upgoing energetic electrons have been observed (both inverted-V and broadband distributions, albeit spatially separated) simultaneously with upgoing broadband emissions interpreted as the whistler mode (Ebert et al., 2017; Elliott et al., 2018a; 2018b; Mauk et al., 2020; Paranicas et al., 2018). There has been ongoing research on plasma processes in this region and this will not be the focus of this study (e.g. Elliott et al., 2020; Shi et al., 2020; Masters et al., 2021).

In this paper, we combine all four instruments (described in the next section) from Juno's fields and particles package to reconcile the various repeatable features exhibited by particle spectra, electric and magnetic field spectra, as well as field-aligned currents across Jupiter's auroral zones.

2. Instruments and Data Description

We utilize four *in-situ* instruments onboard Juno with fields- and particles-measuring capabilities.

The Waves instrument measures an electric field component, E_y, using a 4.8 m tip-to-tip electric dipole antenna that is parallel to the spacecraft *y*-axis (Kurth et al., 2017). Its containment within the spin (*x*-*y*) plane means two electric field components are effectively measured twice per spin with a period of 30 seconds. A magnetic search coil measures a magnetic field component, B_z, using a single sensor mounted along the spacecraft's spin (*z*) axis. We utilize Waves data provided by the Low Frequency Receiver which covers the frequency ranges of 50 Hz – 20 kHz simultaneously for the E- and B-fields at 50 kilosamples per second. This frequency range is sufficient to capture plasma waves well below and above and the proton cyclotron frequency, f_{cH+}, in the near-Jupiter environment, by virtue of the very high magnetic field strength.

This Waves suite provides the capability to distinguish between electrostatic, $\delta E(f) \gg c\delta B(f)$, and electromagnetic, $\delta E(f) \sim c\delta B(f)$, waves below 20 kHz. Furthermore, the Poynting vector direction at a given frequency, $\delta\vec{E}(f) \times \delta\vec{B}(f)/\mu_0$, can be resolved, although incomplete measurement of all three E- and three B-field components means some assumptions are necessary. We mitigate this issue by reasonably assuming that the plasma waves are propagating either almost parallel or anti-parallel to $\overrightarrow{B_0}$. Only one component of the Poynting vector can be resolved, which is along the spacecraft *x*-axis and its sign is compared with the sign of the background magnetic field's *x*-component, B_{0x}. The sign of the Poynting vector component is determined from the mutual phases between E_y and B_z, with the mutual phases $\phi_{Ey\text{-}Bz}$ and coherency, $C_{Ey\text{-}Bz}$ calculated. In the northern hemisphere, the combination of $\phi_{Ey\text{-}Bz} \approx 0°$ (180°) and a positive B_{0x} indicates upgoing (downgoing) plasma waves, i.e., away from (toward) Jupiter. The reverse is true when either B_{0x} is negative or the spacecraft is in the southern hemisphere. This technique has been used at Jupiter to constrain the directionality of lightning-induced rapid whistlers (Kolmašová et al., 2018), plasma waves in Jupiter's aurora (Kurth et al., 2018), as well as Io's Main Alfvén Wing (Sulaiman et al., 2020).

The Jupiter Energetic-particle Detector Instrument (JEDI) measures energetic charged particle distributions. For this study we utilize JEDI's 50 to 1,000 keV electron- and 50 keV to >2,000 keV proton-measuring capabilities. The Jovian Auroral Distributions Experiment (JADE) measures thermal charged particle distributions. We utilize the JADE's 3 to 30 keV electron (JADE-E) and 0.5 to 46 keV/q ion (JADE-I) sensors for H^+. JADE and JEDI complement one another to provide electron and proton energy and pitch angle spectra over a wide energy range. More details on the

instruments can be found in Mauk et al. (2017) and McComas et al. (2017), respectively. Science-ready data techniques and challenges are detailed in Mauk et al. (2020) and Allegrini (2020; 2021).

For the purpose of this study, we calculate the energy flux for electrons and H^+ (see Mauk et al., 2017; Clark et al., 2018; Allergrini et al., 2020). This is given by

$$Energy\ Flux = \pi \int_{E_{min}}^{E_{max}} I \cdot E \, dE \qquad (1)$$

where I is the particle intensity ($cm^{-2}\ s^{-1}\ sr^{-1}\ keV^{-1}$), E is the electron energy (keV) and π is the area-projected-weighted size of the loss cone. The width of the loss cone is estimated as $arcsin(1/R^3)^{1/2}$, where R is the Jovicentric distance in Jovian radii.

The magnetometer instrument (MAG) measures three components of the magnetic field and is used to determine the directionality of field-aligned currents inferred from azimuthal deflections in the magnetic field, δB_ϕ (Connerney et al., 2017). This is achieved by subtracting the modelled internal planetary field (Connerney et al., 2018) and slowly varying trends from the measurements, leaving out the deflections. The very high field strength compared to the average size of the deflections associated with the auroral currents poses challenges and this technique is thoroughly discussed by Kotsiaros et al. (2019). Furthermore, measured magnetic field fluctuations can be transformed into transverse and compressive components to identify the presence of Alfvén waves (Gershman et al., 2019). In our analysis, M-shells (magnetic shells for non-dipolar magnetic fields (McIlwain, 1961)) were calculated by field-line tracing using the JRM09 internal field model (Connerney et al., 2018) with a superimposed external current sheet model (Connerney et al., 1981).

The magnetic field measurements allow JADE and JEDI to order particle counts by pitch angle, thus allowing for particle directionality to be determined. Furthermore, the magnetic field strength is used by Waves to calculate the electron and proton cyclotron frequencies, f_{ce} and f_{cH+}, and this allows for the species' temporal scales to be identified in spectrograms.

This study highlights datasets taken from the early part of *Juno*'s Prime Mission phase when the spacecraft's orbital plane was in the dawn sector (thereby sampling the dusk aurora near perijove). This is due to the approximate orthogonality between Jupiter's magnetic field and *Juno*'s spin vectors, which optimizes pitch angle coverage. The pitch angle coverage was compromised as *Juno*'s orbital plane migrated toward the nightside and will begin to improve as the migration continues into the dusk sector (and sample the dawn aurora near perijove) in the Extended Mission phase.

3. Overview of Fields, Particles, and Plasma Waves in Jupiter's Auroral Zones

We begin by providing an overview of the various fields, particles, and plasma wave phenomena observed when Juno was magnetically connected to (and equatorward of) Jupiter's auroral zones. We analyze four auroral passes which are shown in Figure 1 as ultraviolet (UV) images from the Ultraviolet Spectrograph instrument (Gladstone et al., 2017) with Juno's magnetic footprint track overlaid. Figure 2 shows multi-instrument datasets recorded during Juno's pass of Jupiter's southern aurora after its fourth perijove (PJ4S) corresponding to the aurora shown in Figure 1a. Figures 2a and 2b are electric and magnetic field frequency-time spectrograms, respectively, with

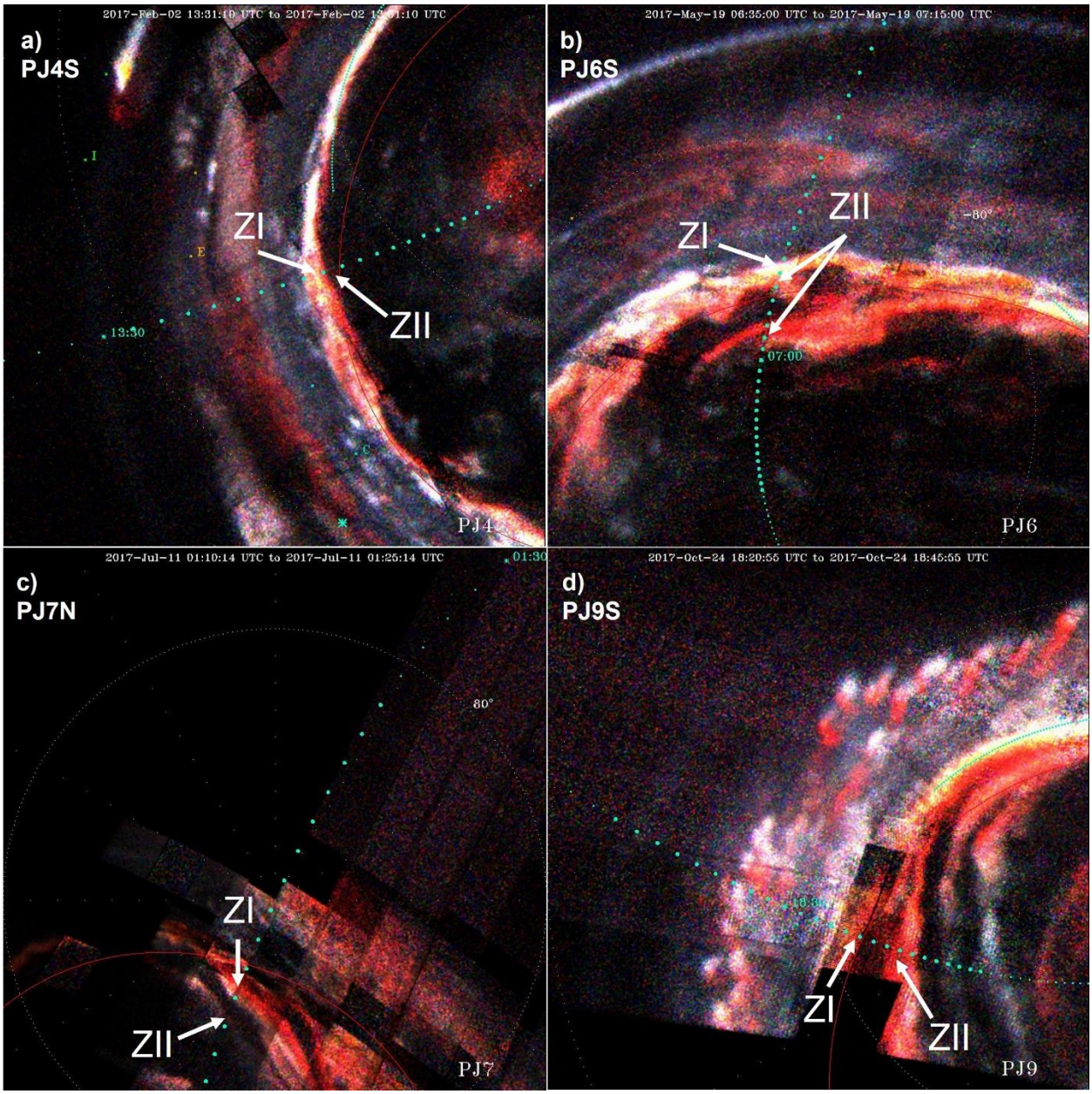

Figure 1 – Orthographic projections of UV images of Jupiter's aurora in false color for each event presented in Figures 2-5. Overlaid are magnetic footprint tracks of Juno separated by one minute.

the H^+ and H_3^+ cyclotron frequency, f_{cH+} and f_{cH3+}, overlaid. Throughout the time interval, f_{cH+} and f_{cH3+} were well within the frequency range of the Low Frequency Receiver (50-20,000 Hz). Such strong magnetic fields have not been previously met by spacecraft. Particularly for sampling auroral field lines, the strength of Jupiter's magnetic field allows the Waves instrument to detect plasma waves at frequencies below f_{cH+} and f_{cH3+}, and thus assess interactions with protons and heavy ions. Figure 2c is a spectrogram of the transverse (non-compressive) magnetic field power recorded by the magnetometer between 0.2 and 5 Hz (Gershman et al., 2019). Overlaid is the perturbation of Jupiter's azimuthal magnetic field, δB_φ, after subtracting the JRM09 internal field model (Connerney et al., 2018). From Ampère's law, significant gradients in the δB_φ perturbations

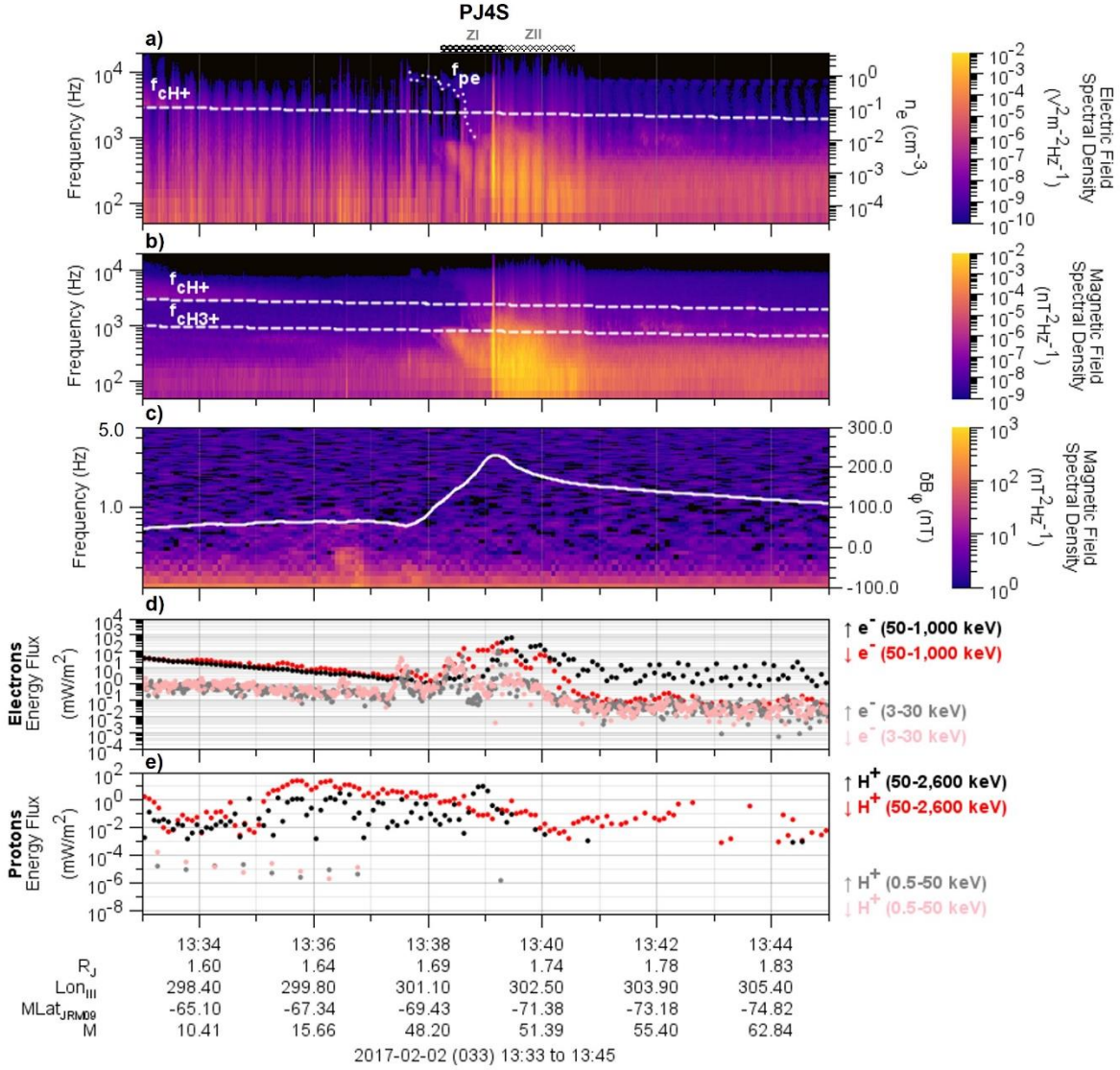

Figure 2 – Plasma waves, fields, and charged particles when Juno was magnetically connected to Jupiter's southern auroral zone near its 4th perijove (PJ4S). (a-b) Electric and magnetic field frequency-time spectrogram, respectively, measured by Waves. Overlaid onto each is the proton cyclotron frequency, f_{cH+}, as white dashed lines. The electron plasma frequency, f_{pe}, is digitized as the lower frequency cutoff of the Ordinary mode and shown as a white dotted line. The y-axis on the right converts f_{pe} in Hz to electron number density, n_e, in cm^{-3}. (c) Transverse magnetic field fluctuations measured by MAG. Overlaid is the perturbation in the azimuthal magnetic field, δB_φ, as a white solid line. (d) Electron energy fluxes measured by JADE (light colors) and JEDI (dark colors) over the energy ranges 3-30 keV and 50-1,000 keV, respectively. Black/gray and red/pink correspond to upward and downward populations, respectively. (e) Proton energy fluxes measured by JADE (light colors) and JEDI (dark colors) over the energy ranges 0.5-50 keV and 50-2,600 keV, respectively. Black/gray and red/pink correspond to upward and downward populations, respectively.

are diagnostic of field-aligned currents (e.g., Kotsiaros et al., 2019). Figure 2d is a time series of the electron energy flux for the lower (3-30 keV) and higher (50-1,000 keV) energy ranges recorded by JADE and JEDI, respectively. These are specifically for populations within the loss cone and are differentiated between upward (away from Jupiter) and downward (toward Jupiter). Similarly, Figure 2e is a time series of the H^+ energy flux covering lower (0.5-50 keV) and higher (50-2,600 keV) energy ranges within the loss cone recorded by JADE and JEDI, respectively.

Describing the data from left to right along Juno's poleward trajectory, magnetic field lines threading Jupiter's diffuse aurora (DifA) were initially sampled, transitioning to Zone-I from 13:38:15, then to Zone-II from 13:39:15 until 13:40:30, after which Juno was in the polar cap. The plasma wave spectra show significant wave power in both the E- and B-fields beginning as Juno entered Zone-I. Below f_{cH3+}, intense electromagnetic waves with a dispersive spectral character, i.e., a frequency dependence with time, extends throughout Zone-I. This is followed by an intense broadband electromagnetic emission that extends throughout Zone-II. There are jumps in both the low-frequency electric and magnetic field spectral densities at the boundary between Zone-I and Zone-II suggesting the mode is not continuous across. There are intermittent bursts of broadband emissions mostly in Zone-II. Above f_{cH+} and from equatorward of Zone-I, an electromagnetic emission is present with a clear lower frequency cutoff that is continuous across and throughout Zone-I. This lower frequency cutoff decreases non-monotonically until Zone-I and extends well below f_{cH+}. Of particular interest is the lack of a clear whistler-mode auroral hiss signature which exhibits a funnel shape above f_{cH+} and is a key plasma wave feature of planetary auroral regions (also commonly known as VLF saucers) (e.g., Gurnett et al., 1983).

The magnetic field data shows intense transverse fluctuations, interpreted as low-frequency Alfvén fluctuations, that extends throughout the region equatorward and stops short of Zone-I. There is likely some evidence of this fluctuation within Zone-I, albeit to a much lesser extent. However, this is near the low-frequency noise level and should be interpreted with care. The strongest field-aligned current, manifested as a large gradient in δB_φ perturbations in a narrow interval, marks the entry into Zone-I. Interestingly, this is clearly separated from the transverse fluctuations, which are largely equatorward of Zone-I. The δB_φ gradient is interpreted as an upward field-aligned current. In Zone-II the gradient reverses, but falls off much more slowly, indicating downward field-aligned current region that is extended over a larger region and is not as ordered and continuous as its Zone-I counterpart.

The electron energy flux shows bidirectional populations in both energy ranges equatorward of Zone-I and asymmetries emerge as Juno enters Zone-I. Just equatorward of the Zone-I boundary, there is a peak in the lower (3-30 keV) energy electron flux with more downward than upward fluxes. This is followed by a clear separation between the fluxes in the higher (50-1,000 keV) energy range in Zone-I with the downward energy fluxes dominating by up to ~100× compared to the upward energy fluxes. In Zone-II the asymmetry in the higher-energy electrons is clearly reversed, with greater upward energy fluxes than downward, also by ~100×.

The data for H^+ energy fluxes are more limited in cadence compared to the electrons. In the higher (50-2,600 keV) energy population, there are episodes of bidirectionality, but the clearest feature is the dominant upward H+ energy fluxes near 13:39 in Zone-I by ~100× compared to the downward energy fluxes.

4. Detailed Analysis and Discussion

Various datasets have identified distinct features observed over Jupiter's main aurora (e.g., Gershman et al., 2019; Kotsiaros et al., 2019; Allegrini et al., 2020; Mauk et al., 2020; Szalay et al., 2017; 2021), however, these are yet to be analyzed altogether, and including a plasma wave analysis, to determine their association between the different zones and, more importantly, how they can be reconciled and fit into the bigger picture of Jupiter's auroral generation mechanisms.

In addition to Figure 2 (PJ4S), we include three more multi-instrument time histories when Juno was magnetically connected to the auroral zones. These are shown in Figures 3-5 for PJ6S, PJ7N, PJ9S, respectively. The format is the same as that of PJ4S, noting that PJ7N is a northern pass and Juno was moving equatorward from left to right. Given the similarities that will be discussed, we do not go through each figure in detail but will highlight certain unique features where necessary. We focus our analysis on Zone-I and Zone-II, which are thought to carry the Birkeland currents.

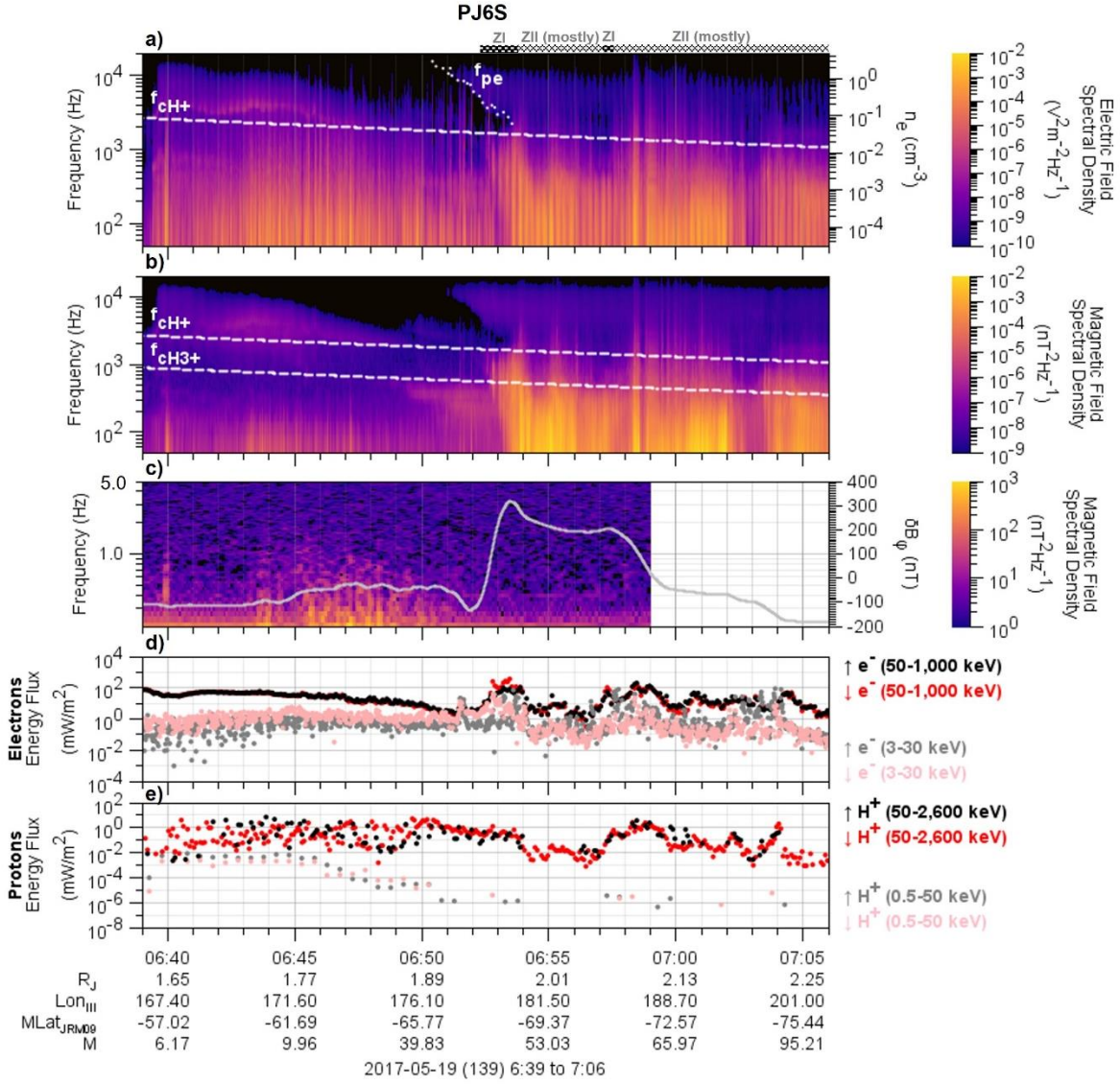

Figure 3 – Same as Figure 2 but for Jupiter's southern auroral zone near its 6th perijove (PJ6S)

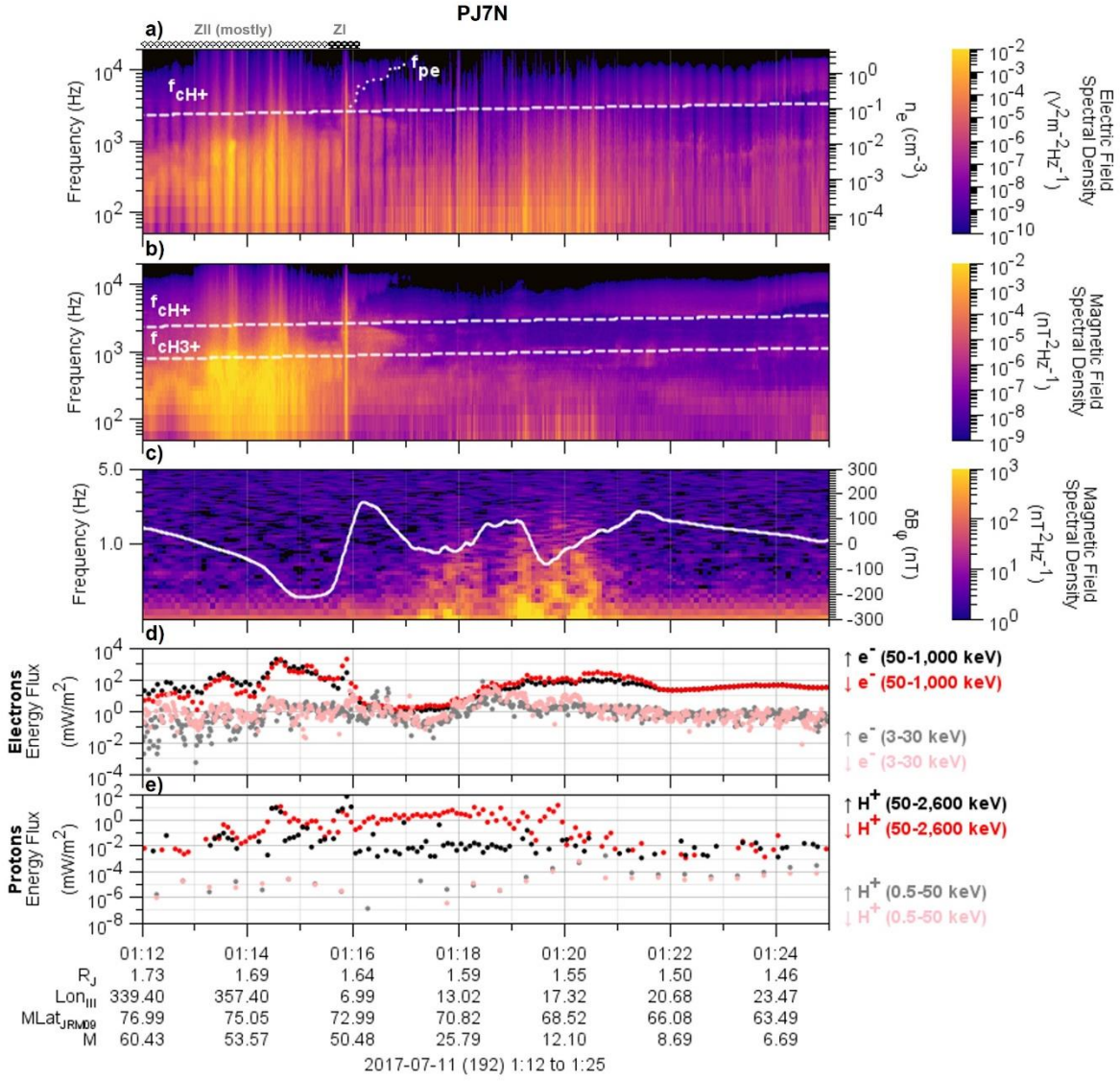

Figure 4 – Same as Figure 2 but for Jupiter's northern auroral zone near its 7th perijove (PJ7N)

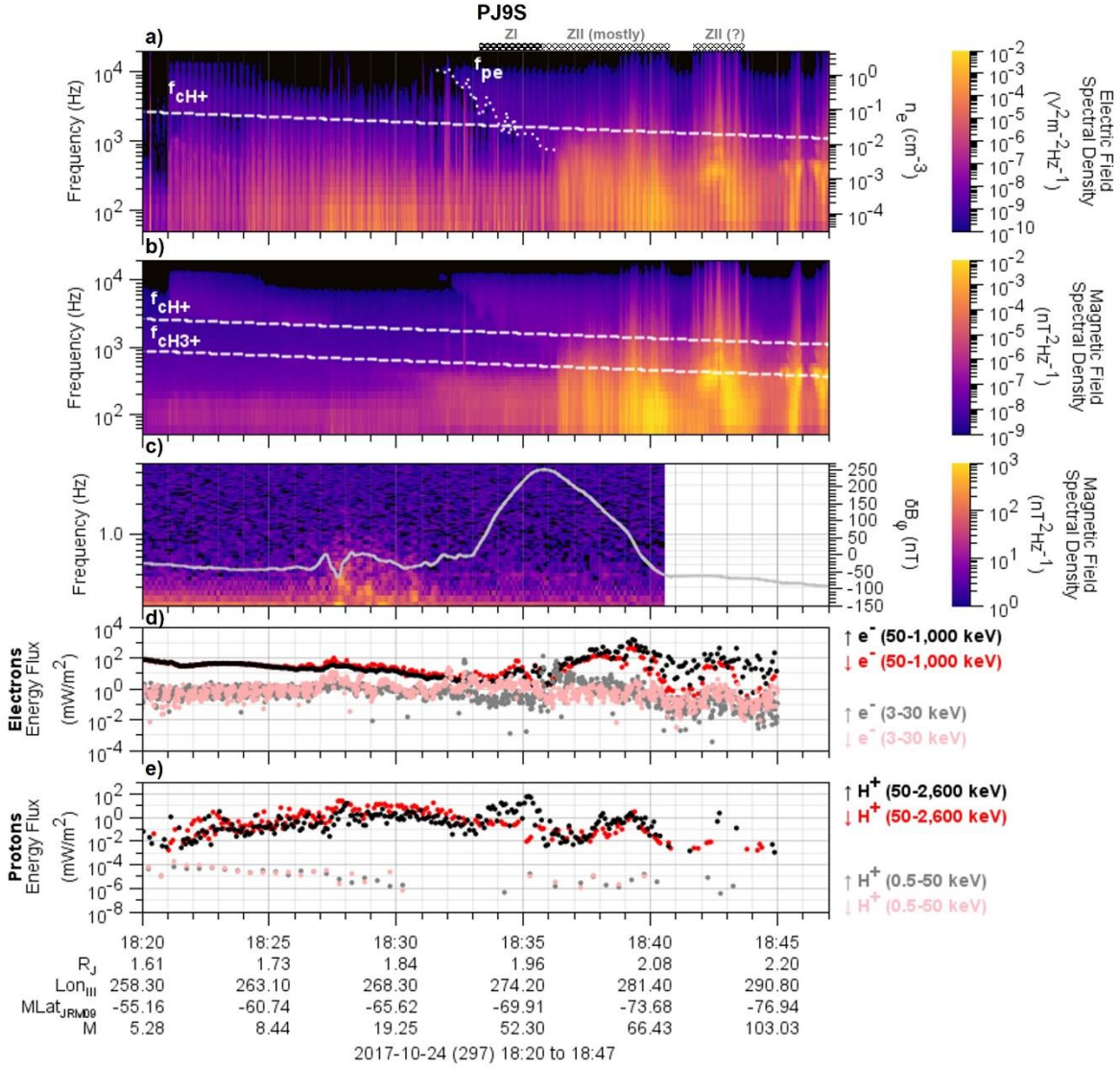

Figure 5 – Same as Figure 2 but for Jupiter's southern auroral zone near its 9th perijove (PJ9S)

4.1 Zone-I

Zone-I occurs at intermediate latitudes just poleward of the diffuse aurora. The exact latitudes depend on hemisphere and local time. This region is by far the narrowest in latitude among the auroral zones as shown in Figure 1, but its clearly defined equatorward and poleward boundaries, as well as the high repeatability among the various datasets, make it the most straightforward to identify. Mauk et al. (2020) characterized this region with dominant downward energetic electrons within the loss cone.

Kotsiaros et al. (2019) and Mauk et al. (2020) noted an agreement between the upward field-aligned current and predominantly downward energetic electrons for the PJ6S auroral pass (shown here in Figure 3), suggesting that Zone-I is associated with upward electric currents. Figures 2-5

corroborate this correspondence between the 50-1,000 keV downward electrons and the well-structured upward field aligned current from δB_φ and confirm that most of the upward current is indeed carried by downward energetic electrons. It should be highlighted that although upward currents in Zone-I are well-ordered, the predominantly downward electron acceleration supporting these currents are via both inverted-V and broadband distributions, often the latter attaining higher energies (Mauk et al., 2017b). These distributions have been observed serially within the same Zone-I pass and are occasionally overlaid onto one another (see Figures 8 and 12 in Mauk et al., (2020)). While the domination of the downward energetic electron is a reliable predictor of Zone-I, there exists large variability in the size of the asymmetry between the downward and upward energy fluxes among the different events. This can be as large as 100× (e.g., PJ4S) and as relatively modest as 3-5× (e.g., PJ6S and PJ9S). The size of the asymmetry is likely related to both the nature of the acceleration region and Juno's proximity to it.

Kurth et al. (2018) showed for PJ7N that an interval of downward broadband electron distribution (in what was later identified as Zone-I) is coincident with brief but very intense broadband plasma waves in both the electric and magnetic spectra (~01:15:51 in Figure 4). It appears that this correspondence is repeatable across events whenever broadband distributions are present, e.g. 13:39:07 during PJ4S in (Figure 2). There are, however, no plasma wave signatures that uniquely correspond to downward inverted V electron distributions. Kurth et al. (2018) proposed the importance of these intense broadband electromagnetic waves in intervals of broadband electron acceleration and determined the direction of their Poynting vector with respect to the Jovian magnetic field to show that they were propagating in the same direction as the predominant downward energetic electrons. These waves were interpreted as being in the whistler mode as the frequency extends well above f_{cH+} and assumed to cut off at the electron plasma frequency, f_{pe}, at ~10 kHz (or $n_e \approx 1.2$ cm^{-3}), which represents the theoretical upper frequency cutoff for whistler-mode waves in the presence of a strong magnetic field. We will show in the next section, however, that Zone-I is a region where the electron densities are dramatically depleted to as low as <0.01 cm^{-3}, or $f_{pe} < 900$ Hz. Densities could not be inferred *within* these brief intervals of broadband acceleration, therefore the presence of the whistler mode would imply that the densities are anomalously greater during these intervals. Broadband electromagnetic waves are routinely observed over Earth's auroral regions, although typically confined to the downward current regions (Ergun et al., 1998b) and have also been reported in Jupiter's polar cap region (Elliot et al., 2020). We will revisit these features and show their correspondences against energy- and pitch-angle-time spectra when discussing Zone-II as they appear to be much more prevalent there.

Another important observation in Zone-I is the lack of, or significant reduction in, Alfvénic fluctuations compared to just equatorward in the diffuse aurora. Alfvén waves are known to develop parallel electric fields when finite electron mass is considered and their role has therefore been posited to explain the broadband nature of Jupiter's auroral electrons (Saur et al., 2018; Lysak et al., 2021). It is therefore likely that these waves have dissipated at higher Zone-I altitudes, lending most of their energy to electron acceleration. It is important to note that Jupiter's low-altitude region is characterized by very strong magnetic fields meaning any Alfvénic fluctuations present may just be too small to be picked up by the magnetometer. The Poynting flux is estimated as $\delta B^2 v_A/\mu_0$, where v_A is the Alfvén speed which considerably rises in the presence of sharp density depletions. Therefore, for a given Poynting flux, it follows that δB_φ would decrease correspondingly.

It is worth emphasizing that the Alfvénic fluctuations are repeatable signatures of the diffuse aurora, but not Zone-I or Zone-II. The waves are clearly supported over a wide range of M-shells. Allegrini et al. (2020) presented a survey showing that the lower-energy 3-30 keV electrons typically peak just equatorward of the main oval (or what is now called Zone-I). It appears from Figures 2-5 that the poleward edge of the Alfvénic fluctuations is when the 3-30 keV electrons peak and precedes the higher 50-1,000 keV that power Zone-I. Interestingly, during PJ4S and PJ7N (Figures 2 and 4) the Alfvénic fluctuations diminish as the 3-30 keV electron energy fluxes peak at ~13:37:30 and ~1:18:30, respectively, before recovering again. Li et al. (2021) applied a data-model comparison to show that whistler-mode waves are the driver of Jupiter's diffuse auroral precipitation above several keV via pitch-angle scattering, although this mechanism did not account for the observed precipitation of lower energies (< several keV) and was limited to lower latitudes (M-shells 8-18). Based on our observed correspondences, we postulate that Alfvén waves may indeed be responsible for precipitating lower energy electrons in the diffuse aurora at the higher latitudes.

The most prominent plasma wave signature in Zone-I are intense emissions below f_{cH+} and f_{cH3+}. The electric and magnetic field spectral densities are enhanced over a broad range of low frequencies (few kHz bandwidth) and undergo a distinct drop in intensity at f_{cH+} and/or at f_{cH3+}. This is usually an indication of strong damping via cyclotron resonance where the wave energy is transferred to the corresponding ions. This characteristic is consistent with ion cyclotron waves and their observation in the presence of upward energetic ions and downward energetic electron beams draws a strong analogy to both Earth's and Saturn's upward current regions where the correlation has been observed (e.g., Cattell et al., 1988; McFadden et al., 1998; Mitchell et al., 2009; Bader et al., 2020). Ion cyclotron waves in the auroral regions have been observed as both electrostatic (EIC) and electromagnetic (EMIC) modes. The strong magnetic component here is evidence that EMIC waves are present, though not necessarily in the absence of EIC, and the significance is that they carry Poynting fluxes.

Figure 6a-d shows an analysis of the Poynting vector direction for these waves during PJ4S. These are the emissions present below 1 kHz and the series of peaks and nulls in the electric field spectrum is due to spin modulations. The electric and magnetic field fluctuations have high coherency, $C_{Ey\text{-}Bz} \approx 1$, and the combination of a phase $\varphi_{Ey\text{-}Bz} \approx$ -180° (or 180°) and a positive $B_x/|B_x|$ in the southern hemisphere indicates an upward-propagating wave. Figure 6e shows that the power of these waves primarily resides perpendicular to the magnetic field. Here we compare the spin-modulations in the electric field spectral densities to the angle between the antenna dipole and background magnetic field and show that spectral densities peak (depress) when the antenna is perpendicular (parallel) to the magnetic field. At the measured frequency of ¼ f_{cH+} the ratio of the components is $E_\perp/E_{||} = 200$. Despite a strong magnetic component, the E/cB ratio (not shown here) is greater than one but of order unity. This can occur in the presence of an admixture of EIC and EMIC waves.

Although we cannot directly verify that they are intrinsically left-hand-polarized, we can indirectly infer this from the fact that their electric and magnetic fields are highly coherent, fluctuate perpendicular to the background magnetic field, and do not propagate above f_{cH+} or f_{cH3+}. Altogether, these are consistent with resonant absorption of left-hand-polarized ion cyclotron waves, a well-recognized mechanism for ion heating (e.g. André et al., 1998; Chang et al., 1986; Lysak, 1986). The observed (mostly) upward-propagation of these waves is somewhat in contrast to what is typically observed during low-altitude passes of Earth's aurora, where waves below f_{cH+}

are more commonly observed to be downward propagating (Gurnett et al. 1984; Chaston et al., 1998). The difference at Jupiter may be either due to their sources originating at an altitude lower than Juno, i.e. $\lesssim$1 R_J above the one-bar level, or a different generation mechanism altogether. Electron drifts as the source of free energy driving ion cyclotron instability have been invoked to explain their correlation with auroral field-aligned currents (Cattell et al., 1998). Testing whether this hypothesis holds at Jupiter requires solving dispersion relations with modelled particle distributions which is beyond the scope of this study. It has been further demonstrated that broadband EMIC waves can also accelerate cold secondary electrons to form counterstreaming field-aligned electrons (McFadden et al., 1998). Since bidirectional electrons are a key feature of Jupiter's auroral zones, the role of EMIC waves should not be neglected.

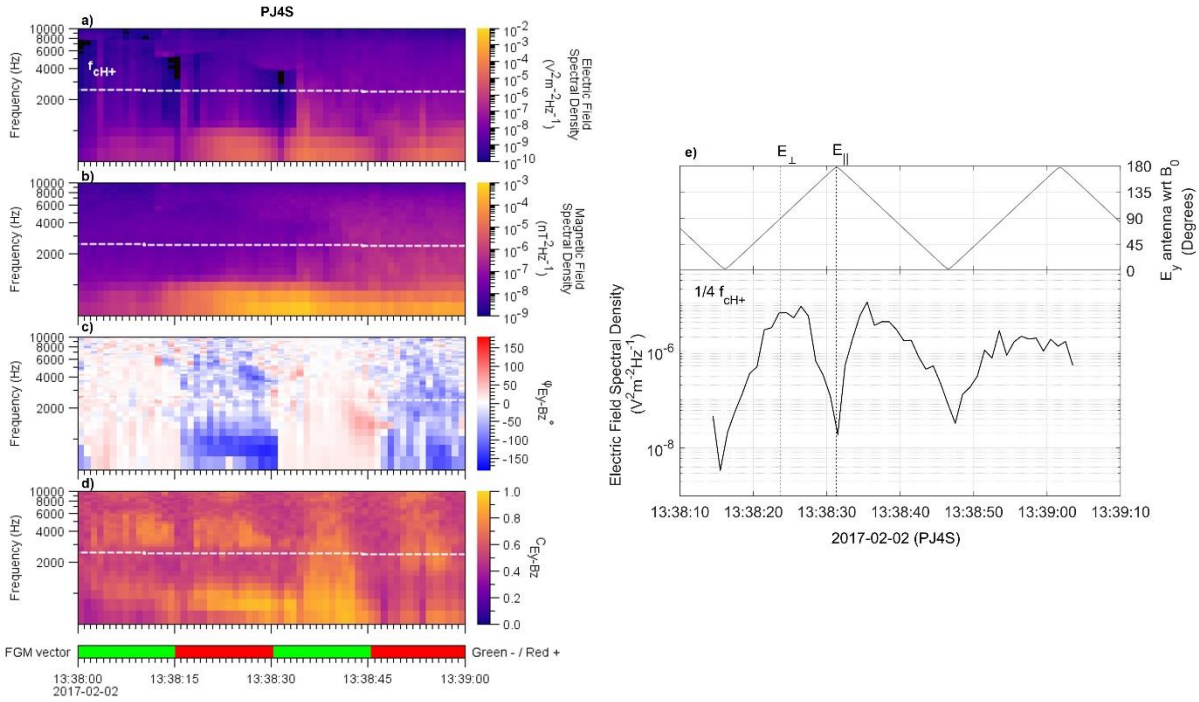

Figure 6 – (left) Poynting vector analysis during PJ4S. (a-b) Electric and magnetic field frequency time spectrograms, respectively. (c-d) phase difference and coherence between measured electric and magnetic fields, respectively. (right) Angle between electric field antenna and background magnetic field correlated against the electric field spectral density at ¼ f_{cH+}

The coincident field-aligned H^+ fluxes suggest that any perpendicular heating by the ion cyclotron waves is not sufficient to deviate the pitch angle from the field-aligned direction and generate conics. The measured electric field spectral density of 10^{-5} V m^{-1} Hz^{-1} near f_{cH+} (Figure 6e) yields a maximum cyclotron resonant heating rate of ~500 eV/s (Chang et al., 1986) and is comparable to that measured in Io's Main Alfvén Wing where, by contrast, H^+ conics were detected (Clark et al., 2020; Sulaiman et al., 2020). The difference is likely due to the interaction time, proximity to, nature of the acceleration region or a combination thereof. Szalay et al. (2021) concluded, based on the presence of H^+ inverted-V distributions, that quasi-static parallel potential structures drove the acceleration of H^+ away from Jupiter's high-latitude ionosphere. This is further supported by

the disappearance of upward H^+ during intervals of broadband acceleration within Zone-I shown by Mauk et al. (2018). The observation of both downward electron and upward H^+ beams at these altitudes would suggest that Juno was in or close to a unidirectional acceleration region, i.e., an upward parallel potential. Therefore, it is possible that the perpendicular heating supplied by ion cyclotron waves are overcome by the action of more powerful parallel potentials that deposit much larger amounts of energy along the field line. The ion cyclotron waves (shown to be upward propagating) may have their source in the ionosphere where the density is high and enough ions exist to significantly dampen the waves. Cold ionospheric ions are bound by Jupiter's large gravitational potential (the gravitation binding energy of H^+ is ~20 eV and H_3^+ is ~60 eV) and in order to be admitted into the electrostatic potential at higher altitudes, a means of energization is required to escape the gravitational potential. When ions are heated perpendicular to the magnetic field in the presence of a diverging magnetic field, they experience a mirror force that transports them to a region of weaker magnetic field, i.e., higher altitudes, as a parallel velocity component develops to conserve kinetic energy and the first adiabatic invariant.

In summary, a multi-instrument in-situ analysis shows that the following criteria identify Zone-I in Jupiter's low-altitude auroral region: (i) presence of a gradient in the B_φ perturbation that is indicative of an upward field-aligned current, as measured by MAG; (ii) greater downward electron energy fluxes than upward, as well as greater than outside the loss cone, accompanied by inverted-V and/or broadband distributions as measured by JEDI; (iii) the low-frequency portion of intense, apparently dispersive, coherent, mostly upward-propagating ion (H^+ and/or H_3^+) cyclotron waves, as measured by Waves; and (iv) presence of field-aligned upward flowing H^+ accompanied by inverted-V distributions, as measured by JADE and JEDI. These observations are unique to Zone-I and highly repeatable, such that any one of them is highly predictive of Zone-I. Furthermore, they exhibit distinct and unambiguous equatorward and poleward edges that are consistent with the main oval emission shown in Figure 1. The boundary at which Alfvénic fluctuations significantly decrease reliably marks the entry into Zone-I from the diffuse aurora. The deficiency in observed Alfvénic fluctuations, however, is not a unique marker of Zone-I as this is continuous into Zone-II.

4.2 Electron density depletions in Zone-I

Electron density depletions occur within Zone-I, exhibiting large variability and with a sharply defined equatorward edge. The scatter plot in Figure 7a shows the electron number density variation with increasing M-shell. This is color-coded in altitude over a range of 0.6 – 1.7 R_J above the one-bar level. The direction of increasing M-shell translates into Juno sampling the auroral regions in the poleward sense, beginning with the equatorward edge of the broad diffuse aurora through to the poleward edge of Zone-I. The M-shells here are likely overestimated since the auroral regions are believed to be mapped to ~30 R_J in the equatorial plane. The purpose of this figure is to examine how the electron densities vary on different field lines, including those mapped to the auroral zones. It should be noted that a different internal and/or current sheet models will yield different M-shell values. We therefore identify the auroral crossings based on *in-situ* observations and not rely on the values provided by M-shell mapping.

We digitize the densities by identifying Ordinary (O) mode waves that are sometimes present during the auroral passes (see Sulaiman et al. (2021) for the theoretical background as well as early and more recent implementations of this technique by Gurnett & Shaw (1973) and Elliott et al. (2021)). The waves are evanescent below f_{pe} and therefore exhibit a low frequency cutoff, as shown

in the first panels of Figures 2-5. Strictly speaking, this cutoff is an upper limit to the local electron plasma frequency due to the possibility of a higher-density region existing between the source and the spacecraft. When this occurs, the measured cutoff corresponds to the maximum density between the source and the spacecraft; however, the cutoffs observed here are usually well-defined and continuous which suggest the densities are local. Since $f_{pe} \propto \sqrt{n_e}$, the total electron number density is straightforwardly obtained and this is in excellent agreement with the electron partial density derived by JADE for overlapping intervals (see Figure S1). Despite the limited coverage in altitude shown here, the expected anti-correlation between density and altitude is present, giving confidence in our method. We obtain density measurements whenever the O-mode waves are present and discernible. The circled points highlight measurements taken when Juno was magnetically connected to Zone-I using all the criteria whenever the O-mode was present during the first 10 perijoves and only criteria (iii) thereafter, when the pitch angle coverage was suboptimal. Recall that any one of the criteria alone is a sufficient marker of Zone-I.

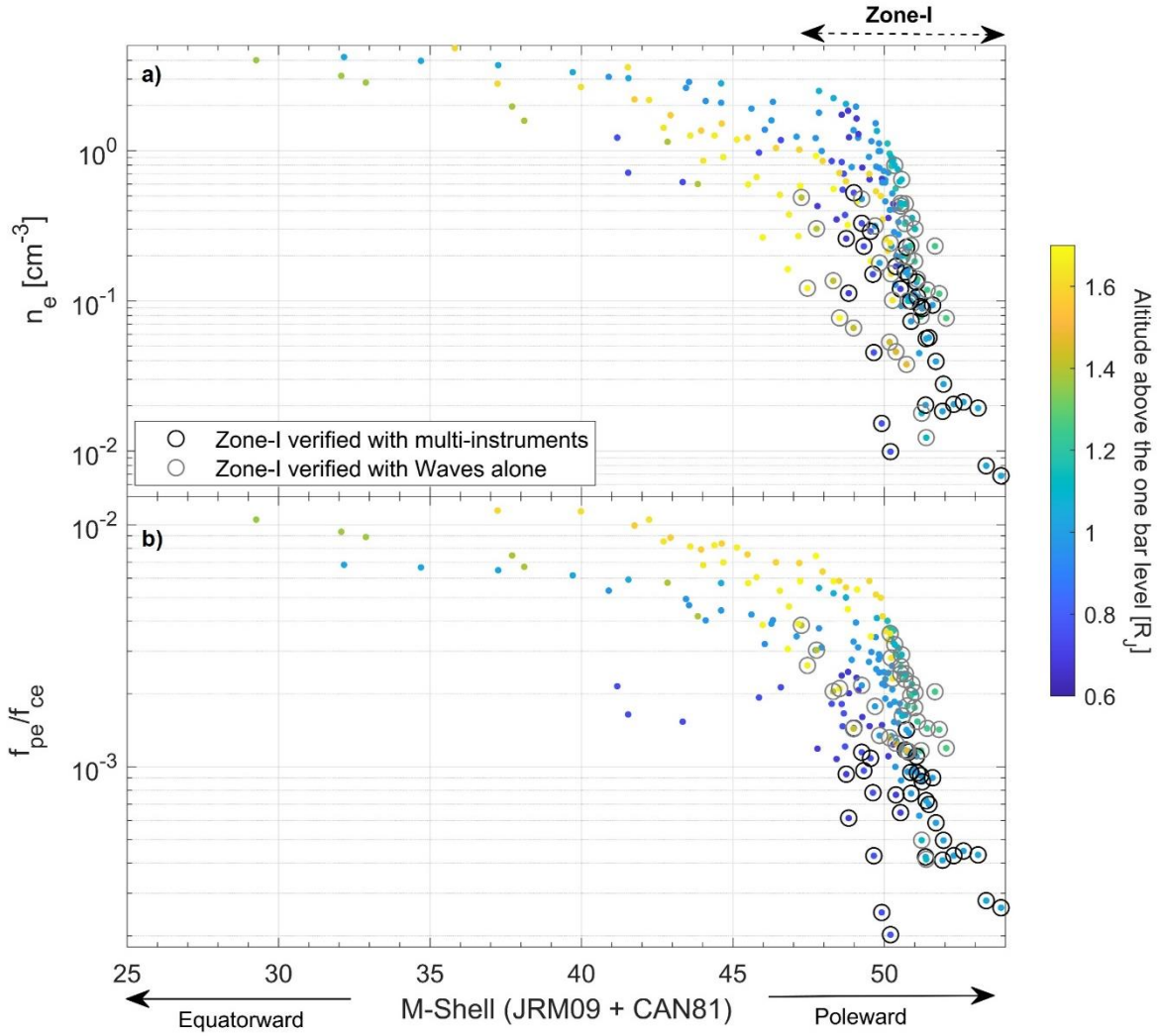

Figure 7 – (a) Electron number density plotted against M-shell and color-coded with Juno's altitude above Jupiter's one-bar level. The circled data points are when Juno was magnetically connected to Zone-I. (b) f_{pe}/f_{ce} plotted against M-shell, same format as (a). The

M-shell was calculated using the JRM09 internal field model (Connerney et al., 2018) + an external current sheet model (Connerney et al., 1981). This is likely overestimating the true M-shell.

Figure 7a exposes a sharply defined boundary between the diffuse aurora and Zone-I. Within Zone-I, the electron densities deplete steeply by up to two orders of magnitude down to below 0.01 cm^{-3}. In Zone-II, the sub-f_{cH+} band of the O-mode waves become "washed out" in the spectrogram due to the presence of intense broadband low-frequency electromagnetic emissions, therefore it is not possible to determine, based on this technique, how far they remain depleted and whether/where they steeply recover. All Zone-I verified densities are below 0.1 cm^{-3} with a subset below 0.01 cm^{-3}.

Density depletions are known to be intimately related to auroral acceleration processes (e.g., Persoon et al., 1998; Paschmann et al., 2003) and are in fact a prerequisite. Their association is well supported by theoretical modelling (Block and Fälthammar, 1968; Knight, 1973) and repeatedly corroborated by experimental evidence (Ergun et al., 2002; Hull et al., 2003) although much of the focus has been on the development of parallel potentials in the context of inverted V distributions. The basic principle is that density depletions reduce the number of charge carriers thereby limiting the ability of plasmas to carry strong field-aligned currents. This "current choke" results in the development of parallel electric fields as the displacement current term of Ampère's law builds up to ensure $\nabla \times \mathbf{B}$ is balanced (Song and Lysak, 2006; Ray 2009).

Although turbulence-induced broadband processes are typically associated with weaker Alfvénic aurora at Earth, they are believed to be of at least equal importance in generating Jupiter's most intense aurora (Clark et al., 2018; Saur et al., 2018). Parallel electric fields from Alfvén waves become important when the $k_\perp^2\lambda_e^2$ term is large, where λ_e is the electron inertial length given by $c/2\pi f_{pe}$ and $k_\perp$ is the wave vector component perpendicular to the background magnetic field. A large $k_\perp$ can be satisfied by a converging flux tube as the area is inversely proportional to B. A low-density region, or greater λ_e, means Alfvén waves undergoing a turbulent cascade are dissipated 'earlier' in k-space. The measured densities in Zone-I equate to λ_e as large as 50 km, larger than 20-30 km modelled by Saur et al. (2018), thereby further lowering the threshold for Alfvénic dissipation to be achieved in the high-latitude region. Dispersive Alfvén waves have been observed within deep density cavities over Earth's auroral oval together with upgoing transversely heated ionospheric ions and downgoing field-aligned electrons. This has been interpreted as evidence for a positive feedback mechanism, whereby small-scale Alfvén waves erode the auroral ionosphere by facilitating ion outflow, which in turn leads to deeper density cavities that maintain the production of small-scale Alfvén waves via refraction and phase mixing of incoming large-scale Alfvén waves (Rankin et al., 1999; Chaston et al., 2006). More recently, Lysak et al. (2021) proposed that an ionospheric Alfvénic resonator (IAR) operating at Jupiter can account for the observed broadband electron distributions. This is a widely accepted model used to explain similar distributions in the case of Earth, whereby the propagation of Alfvén waves is facilitated by a rapid decrease in density (Lysak et al., 1991). The corresponding increase in Alfvén speed gives rise to partial reflection of Alfvén waves which become trapped. At large enough $k_\perp$, the parallel electric field fluctuating at some resonant frequency can result in electron acceleration over a broad range of energies.

Figure 7b combines the electron densities with measured magnetic field strengths to express f_{pe}/f_{ce} variations. This ratio is especially important for the generation of radio emissions via the Cyclotron

Maser Instability (Wu & Lee, 1979). This mechanism requires $f_{pe}/f_{ce} \ll 1$ in the presence of a positive gradient in the perpendicular velocity distribution of weakly relativistic electrons. It is clear that the necessary low f_{pe}/f_{ce} is well satisfied, particularly in Zone-I, thus will provide further constraints on Jupiter's radio sources (e.g. Imai et al., 2019; Louis et al., 2019).

4.3 Zone-II

Among the three zones, Zone-II occurs at the highest latitudes just poleward of Zone-I. This region has a clearly defined equatorward boundary, but its poleward boundary with the polar cap is often ambiguous. Mauk et al. (2020) characterized this region with upward energetic electrons with energy fluxes greater than or equal to the downward component within the loss cone. Another key difference is the bidirectional electrons are almost always broadband in energy. On the other hand, downward H^+ inverted-Vs have been observed intermittently and, by contrast to Zone-I's highly field-aligned H^+ beams, exhibit a nearly isotropic pitch angle distribution with an empty upward loss cone (Mauk et al., 2020). Whereas Zone-I features are typically (but not always) continuous within its boundaries, Zone-II features are spatially or temporally sporadic.

Kotsiaros et al. (2019) and Mauk et al. (2020) noted agreements between the downward field-aligned currents and Zone-II during the PJ6S auroral pass (Figure 3), although this is usually limited to the most intense portion of the energetic particles and not as simple as the ordering for Zone-I. Again, Figures 2-5 corroborate this correspondence. Observed Alfvénic fluctuations in Zone-II remain relatively low/absent and comparable to Zone-I. This could also be evidence of dissipation, especially in a region supported predominantly by broadband, bidirectional energetic electrons (Saur et al., 2018; Lysak et al., 2021) and in the absence of strong evidence for inverted-Vs and thus local parallel potentials. The plasma wave emissions, on the other hand, are the most intense of all zones with the largest average amplitudes in both the electric and magnetic fields. These are present throughout Zone-II and majority of the power is confined to frequencies below f_{cH+} (Figures 2-5), and are often accompanied by brief, intense emissions that extend well above f_{cH+} that resemble those sometimes observed in Zone-I. The difference is that these brief and intense emissions occur intermittently in Zone-I whereas they appear to be a key feature of Zone-II and are correlated with the intervals of most intense energetic electrons which are in turn correlated with downward currents.

The downward current region is fundamentally different from its upward counterpart. The charge carriers are abundantly sourced from the cold, dense ionosphere as electrons and are accelerated by many orders of magnitude above their thermal energy. What is peculiar about Jupiter's Zone-II is that although the downward electron energy fluxes are generally no greater than the upward energy fluxes, they can be as intense or greater than the downward energy fluxes in Zone-I and sufficient to produce observable auroras (Mauk et al., 2020; and see Figure 1 here), in contrast to the "black aurora" at Earth and Saturn that are connected to flux tubes carrying downward currents. It is clear based on the difference in fields and particles characteristics that the acceleration mechanism in Zone-II is distinct and more observationally complicated than that supporting Zone-I. While Juno does not carry a DC electric field instrument, the various characteristics highlighted in the previous section support the sporadic presence (although not exclusively) of parallel potential structures in Zone-I. Other than the downward H^+ inverted Vs that are sometimes observed in Zone-II and not least that they are quasi-isotropic, the evidence for a stable parallel potential is inconclusive. The bidirectional electrons might be interpreted as originating from

potential structures above and below the spacecraft, however, this is not consistent with their broadband energy.

We emphasized in the previous section that EMIC waves should not be neglected in the context of electrons since their link has been established (McFadden et al., 1998), whereby cold secondary electrons are trapped and accelerated to form counterstreaming populations. It is therefore probably not a coincidence that the most intense waves below f_{cH+} occur in Zone-II, where bidirectional electrons are present.

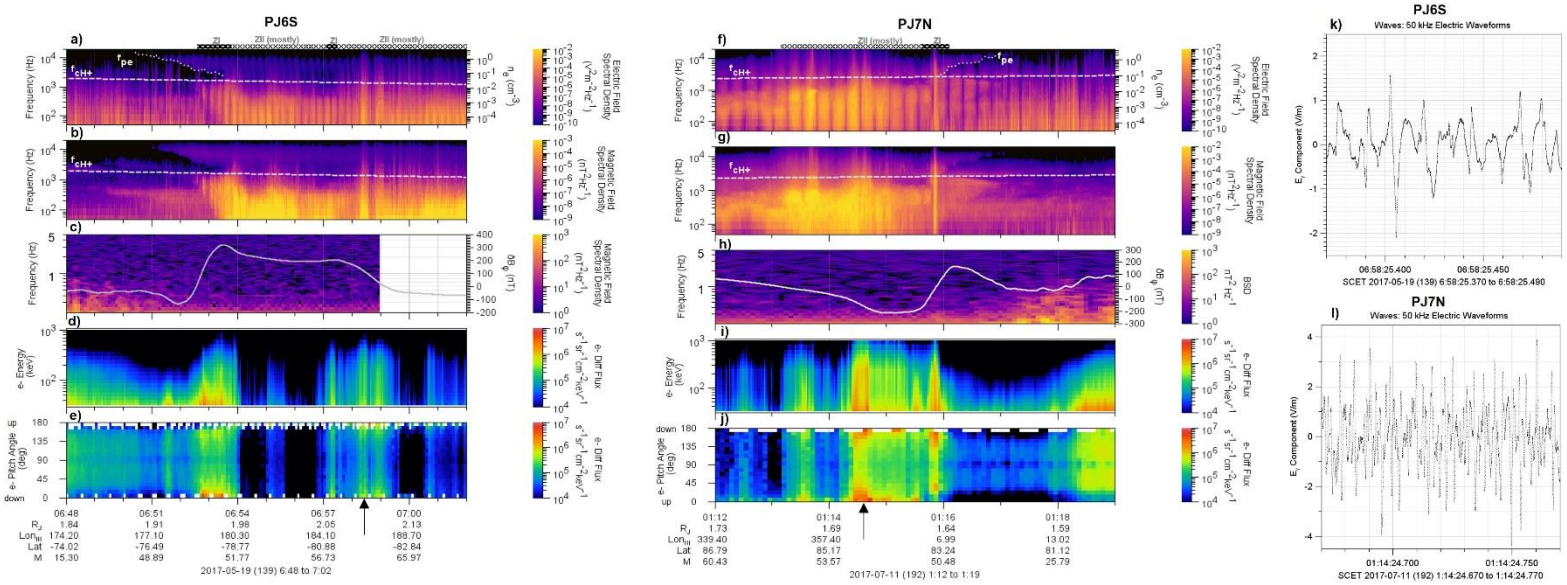

Figure 8 – Plasma waves, fields, and charged particles when Juno was magnetically connected to Jupiter's southern auroral zone near its 4th perijove (PJ4S, left) and Jupiter's northern auroral zone near its 7th perijove (PJ7N, right). (a/f) Electric and (b/g) magnetic field frequency-time spectrogram measured by Waves. Overlaid onto each is the proton cyclotron frequency, f_{cH+}, as white dashed lines. The electron plasma frequency, f_{pe}, is digitized as the lower frequency cutoff of the Ordinary mode and shown as a white dotted line. The y-axis on the right converts f_{pe} in Hz to electron number density, n_e, in cm^{-3}. (c/h) Transverse magnetic field fluctuations measured by MAG. Overlaid is the perturbation in the azimuthal magnetic field, δB_φ, as a white solid line. (d/i) 50-1,000 keV electron energy-time and (e/j) pitch-angle-time spectrograms measured by JEDI. The depletion near 90° is likely due to spacecraft shadowing and therefore not real. (k/l) Electric field waveforms corresponding to the times indicated by black arrows in stack plots.

An important piece of the puzzle for broadband electrons may be in the contemporaneous broadband emissions shown in Figure 8. In the frequency domain, large-amplitude solitary structures (or "spiky" features) in the waveform manifest as broadband noise. Electrostatic solitary waves (ESWs) have been proposed to play a key role in accelerating electrons by carrying substantial potentials and are most often observed in Earth's downward current regions and in the presence of density depletions (Ergun et al., 1998b; Temerin et al., 1982). The ubiquity of these broadband emissions in Zone-II might be explained by the highly nonlinear evolution of two-stream electron beam instabilities, set up by bidirectional populations, that give rise to sharp pulses

in the electric field (Matsumoto et al., 1994), as shown in Figure 8. Field-aligned electrons are then accelerated to a broad range of energies by the sum of individual micro-potential drops as they travel through ESWs. Despite their electrostatic nature, it is possible to measure an associated magnetic component (not shown here) which would result from the Lorentz field of a travelling charge.

Although the electron densities cannot be inferred within Zone-II, we can say with reasonable confidence that they remain low. The O-mode emissions above f_{cH+} appear continuous well into Zone-II with its low frequency edge in the region below f_{cH+} that is dominated by intense electromagnetic turbulence. We therefore set f_{cH+} to be the approximate upper limit of f_{pe} and conclude that the electron densities within Zone-II are < 0.1-0.01 cm^{-3}. Therefore, the correspondingly large electron inertial lengths in Zone-II would similarly lower the threshold for Alfvénic dissipation, which remains the leading mechanism to account for the observed electron spectra (Saur et al., 2018; Lysak et al., 2021). Whether the densities are comparable to Zone-I, of similar variability and/or spatial scales are important questions that are beyond the reach of our current digitization methods.

Perhaps the most recognizable and commonly observed plasma wave feature above auroral regions is the whistler-mode auroral hiss. In a frequency-time spectrogram, they are easily identified by their characteristic funnel or V-shape (Gurnett, 1966; James 1976) which arises when the wave normal angle approaches the whistler-mode resonance cone (Santolík and Gurnett, 2002). The favored generation mechanism is a coherent beam-plasma instability at the Landau velocity (Maggs, 1976; Farrell et al., 1989), i.e., $\omega/k_{\|} \approx v_{\|}$. Since the auroral regions, including satellite auroral flux tubes, are a site for electron beams, whistler-mode auroral hiss are often observed and are often a reliable diagnostic for field-aligned currents (Gurnett et al. 1983; 2009; Sulaiman et al., 2018; 2020). That said, these plasma wave features are not as clearly identifiable in Jupiter's low-altitude auroral zones, contrary to expectation.

Figure 9 shows a rare example when this was observed in the southern auroral zone during PJ12S. Although it appears like there are two similar emissions above and below f_{cH+}, they are fundamentally different and not connected since, above f_{cH+}, the timescales fall below the ion gyroperiod and the ions are effectively unmagnetized. Typically, whistler-mode auroral hiss is not seen to propagate down to as low as f_{cH+}. Along the resonance cone, the lower hybrid frequency, f_{LH}, represents a lower limit through which they cannot propagate but instead reflect. In this highly magnetized regime, i.e., $f_{ce} \gg f_{pe}$, we find $f_{LH} \simeq f_{cH+}$ (Sulaiman et al., 2021) and therefore conclude the waves are reflecting at the f_{cH+} boundary. While the whistler mode is typically observed as electromagnetic, its propagation along the resonance cone is quasi-electrostatic and this is supported by the relatively weaker magnetic component and an E/cB ratio of ~10. This mode is characterized by an index of refraction that is much greater than unity, i.e., a phase velocity that is low. Therefore, the Landau resonance condition requires low-energy electrons for the beam-plasma instability. Higher-energy electrons that interact with higher phase velocities can generate electromagnetic waves that cease to exhibit the characteristic funnel-shape. And even higher energies that exceed the maximum phase speed allowed by the dispersion relation will result in no Landau resonance altogether. This likely explains why quasi-electrostatic auroral hiss is not as common a feature at Jupiter's low-altitude region as at Earth or Saturn owing to the much higher electron energies at play.

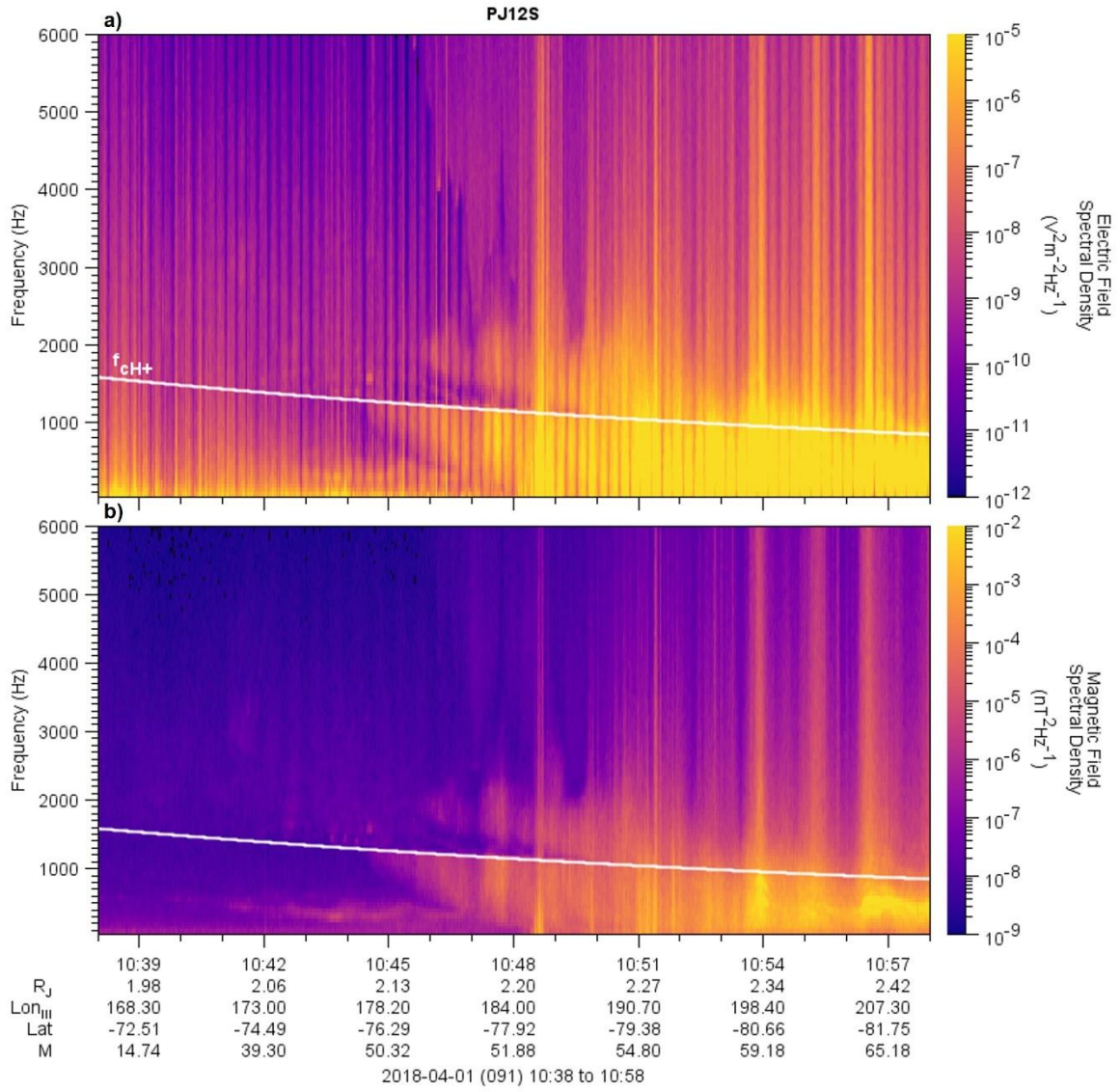

Figure 9 – (a) Electric and (b) magnetic field frequency-time spectrograms when Juno was magnetically connected to Jupiter's southern auroral zone near its 12th perijove (PJ12S) showing the characteristic funnel-shaped whistler-mode auroral hiss above f_{cH+}.

Finally, what has not been covered in this study are the properties of heavy ions. The clear cutoff of plasma waves in Zone-I at f_{cH3+} is indicative of H_3^+ cyclotron waves and is strong (indirect) evidence for presence of upward H_3^+. However, H_3^+ ions in the auroral zones have not been reported by the particle instruments at the time of writing. The presence of multiple heavy ions would have a significant impact since each additional ion introduces five characteristic frequencies: the standard cyclotron and plasma frequencies plus the more complex ion hybrid, multi-ion cutoff, and crossover frequencies, which require numerical solving. The latter three are highly sensitive to the fractional abundance of ions, let alone any individual density. This also means that composition can be constrained by modelling and correctly diagnosing wave modes and their characteristic frequencies. The significance of an ion hybrid frequency in a

multicomponent plasma is that it modifies the wave mode's dispersion relation and therefore how it propagates through the medium. For example, a resonance cone can develop above each hybrid frequency (Santolík et al., 2016). The crossover frequency is that which the waves reverse their intrinsic polarization (left to right or vice versa) and can therefore affect the nature of wave-particle interactions.

5. Summary and Conclusions

We have provided a multi-instrument analysis on Jupiter's low-altitude Zone-I and Zone-II. Figure 10 is a graphical listing of the various observables identified in Zone-I and Zone-II, with the caveat that these structures are likely more complex and may exhibit considerable spatial and/or temporal variability, for example during transient episodes like dawn storms (Bonfond et al., 2021; Ebert et al., 2021). As the spacecraft migrates to afford coverage of the low-altitude dawn aurora, spatial variability of the fields, particles, and plasma wave features will likely arise.

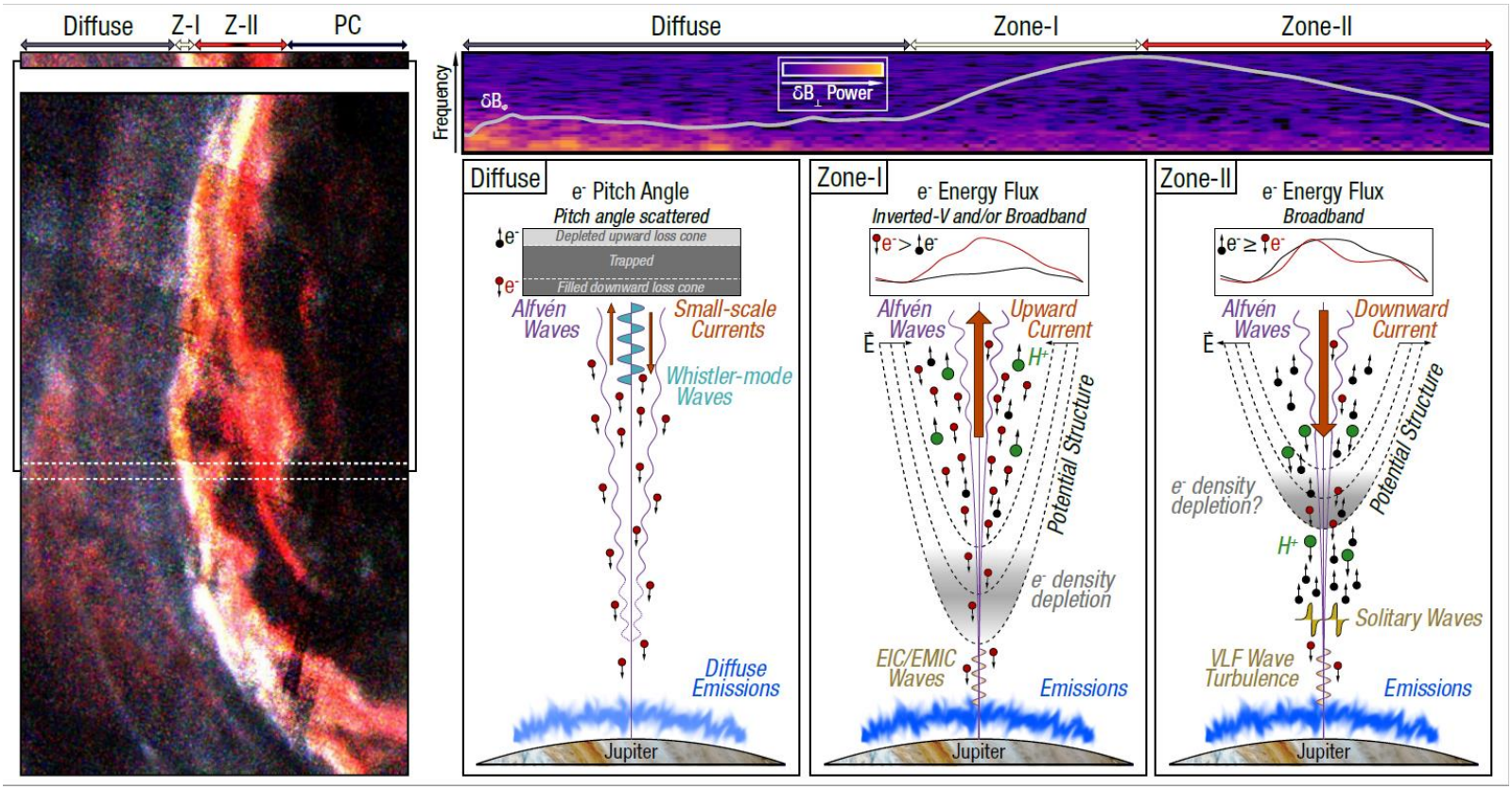

Figure 10 – Graphic illustrating the average picture of the fields, particles, and plasma waves in Jupiter's low-altitude diffuse aurora, Zone-I, and Zone-II.

Our main conclusions are:

- Zone-I and Zone-II are corroborated to be associated with the upward and downward current regions, respectively.
- Alfvénic fluctuations are most profoundly observed in the diffuse aurora and not in Zone-I and Zone-II. In the diffuse aurora, they intermittently diminish where 3-30 keV electron energy fluxes peak and are mostly absent in the Zone-I and Zone-II, where 50-1,000 keV

684 electron energy fluxes dominate. We suggest that this pattern is consistent with Alfvénic
685 dissipation at higher altitudes.
686 • The features of Zone-I are typically coherent across all fields, particles, and plasma wave
687 observations. The equatorward and poleward boundaries are well defined.
688 • The features of Zone-II are typically episodic across all observables. The equatorward edge
689 (with Zone-I) is well defined but the poleward edge with the polar cap can often be
690 ambiguous.
691 • The most prominent plasma wave modes are below the H^+ and H_3^+ cyclotron frequencies,
692 f_{cH+} and f_{cH3+}. Electromagnetic ion cyclotron waves, and possibly including electrostatic
693 waves, are commonly observed in Zone-I and in the presence of H^+ beams. They are
694 typically upward propagating and fluctuate perpendicular to the magnetic field. We
695 interpret them as the means by which gravitationally bound H^+ and H_3^+ can be energized
696 and admitted into a parallel potential at higher altitudes.
697 • Low-frequency plasma waves in Zone-II are the most intense. Electromagnetic emissions
698 are also prevalent in Zone-II where broadband energetic electrons peak, which is in turn
699 correlate with deflections in δB_φ. These are prevalent in Earth's downward current regions.
700 We demonstrate that they are a result of large-amplitude solitary waves. These have
701 previously been shown to be the stable end-result of a two-stream instability and are
702 capable of supporting parallel potentials (Matsumoto et al., 1994). We therefore suggest
703 this likely explains their presence in a zone dominated by bidirectional populations.
704 • Using plasma wave spectra, large-scale electron density depletions are identified over the
705 auroral zones with a sharp boundary between the diffuse aurora and Zone-I. These
706 depletions are critical for the development of high-latitude parallel potentials, Alfvénic
707 dissipation, and radio wave generation.

708

709 **Acknowledgements**

710 The authors gratefully acknowledge J. Faden and the use of Autoplot. The research at the
711 University of Iowa was supported by NASA through contract 699041X with the Southwest
712 Research Institute. OS acknowledges support from the LTAUSA17070 project and from the
713 Praemium Academiae Award. The Waves, JADE, MAG, and JEDI data used in this article have
714 the Dataset ID JNO-E/J/SS-WAV-3-CDR-BSTFULL-V1.0, JNO-J/SW-JAD-3-CALIBRATED-
715 V1.0, JNO-J-3-FGM-CAL-V1.0, and JNO-J-JED-3-CDR-V1.0 respectively and are publicly
716 accessible through the Planetary Plasma Interactions Node in the Planetary Data System
717 (https://pds-ppi.igpp.ucla.edu/). In this paper we use an effective E-field antenna length of 0.5 m.

718

719

720

721

722

References

Allegrini, F., Bagenal, F., Bolton, S., Connerney, J., Clark, G., Ebert, R. W., et al. (2017). Electron beams and loss cones in the auroral regions of Jupiter. *Geophysical Research Letters*, 44(14), 7131–7139. https://doi.org/10.1002/2017GL073180

Allegrini, F., Gladstone, G. R., Hue, V., Clark, G., Szalay, J. R., Kurth, W. S., et al. (2020a). First Report of Electron Measurements During a Europa Footprint Tail Crossing by Juno. *Geophysical Research Letters*, 47(18), e2020GL089732. https://doi.org/https://doi.org/10.1029/2020GL089732

Allegrini, F., Kurth, W. S., Elliott, S. S., Saur, J., Livadiotis, G., Nicolaou, G., et al. (2021). Electron Partial Density and Temperature Over Jupiter's Main Auroral Emission Using Juno Observations. *Journal of Geophysical Research: Space Physics*, 126(9), e2021JA029426. https://doi.org/10.1029/2021JA029426

André, M., et al. (1998), Ion energization mechanisms at 1700 km in the auroral region, *Journal of Geophysical Research*, 103, A3, doi:10.1029/97JA00855

Auroral density fluctuations on dispersive field line resonances. (1999). *Journal of Geophysical Research: Space Physics*, 104(A3), 4399–4410. https://doi.org/10.1029/1998JA900106

Bader, A., Badman, S. V., Ray, L. C., Paranicas, C. P., Lorch, C. T. S., Clark, G., et al. (2020). Energetic Particle Signatures Above Saturn's Aurorae. *Journal of Geophysical Research: Space Physics*, 125(1), e2019JA027403. https://doi.org/10.1029/2019JA027403

Block, L. P., & Fälthammar, C.-G. (1968). Effects of field-aligned currents on the structure of the ionosphere. *Journal of Geophysical Research* (1896-1977), 73(15), 4807–4812. https://doi.org/10.1029/JA073i015p04807

Bonfond, B., Gladstone, G. R., Grodent, D., Greathouse, T. K., Versteeg, M. H., Hue, V., et al. (2017). Morphology of the UV aurorae Jupiter during Juno's first perijove observations. *Geophysical Research Letters*, 44(10), 4463–4471. https://doi.org/10.1002/2017GL073114

Bonfond, B., Yao, Z. H., Gladstone, G. R., Grodent, D., Gérard, J.-C., Matar, J., et al. (2021). Are Dawn Storms Jupiter's Auroral Substorms? *AGU Advances*, 2(1), e2020AV000275. https://doi.org/10.1029/2020AV000275

Carlson, C. W., Pfaff, R. F., & Watzin, J. G. (1998). The Fast Auroral SnapshoT (FAST) Mission. *Geophysical Research Letters*, 25(12), 2013–2016. https://doi.org/10.1029/98GL01592

Cattell, C., Bergmann, R., Sigsbee, K., Carlson, C., Chaston, C., Ergun, R., et al. (1998). The association of electrostatic ion cyclotron waves, ion and electron beams and field-aligned currents: FAST observations of an auroral zone crossing near midnight. *Geophysical Research Letters*, 25(12), 2053–2056. https://doi.org/10.1029/98GL00834

Chang, T., et al. (1986), Transverse acceleration of oxygen ions by electromagnetic ion cyclotron resonance with broad band left-hand polarized waves, *Geophysical Research Letters*, 13, doi:10.1029/GL013i007p00636

761 Chaston, C. C., Ergun, R. E., Delory, G. T., Peria, W., Temerin, M., Cattell, C., et al. (1998).
762 Characteristics of electromagnetic proton cyclotron waves along auroral field lines observed by
763 FAST in regions of upward current. *Geophysical Research Letters*, 25(12), 2057–2060.
764 https://doi.org/10.1029/98GL00513

765 Chaston, C. C., Salem, C., Bonnell, J. W., Carlson, C. W., Ergun, R. E., Strangeway, R. J., &
766 McFadden, J. P. (2008). The Turbulent Alfvenic Aurora. *Physical Review Letters*, 100(17),
767 175003. https://doi.org/10.1103/PhysRevLett.100.175003

768 Clark, G., Mauk, B. H., Haggerty, D., Paranicas, C., Kollmann, P., Rymer, A., et al. (2017).
769 Energetic particle signatures of magnetic field-aligned potentials over Jupiter's polar
770 regions. *Geophysical Research Letters*, 44(17), 8703–8711.
771 https://doi.org/https://doi.org/10.1002/2017GL074366

772 Clark, G., Mauk, B. H., Kollmann, P., Szalay, J. R., Sulaiman, A. H., Gershman, D. J., et al.
773 (2020). Energetic Proton Acceleration Associated With Io's Footprint Tail. *Geophysical*
774 *Research Letters*, 47(24), e2020GL090839.
775 https://doi.org/https://doi.org/10.1029/2020GL090839

776 Clark, G., Tao, C., Mauk, B. H., Nichols, J., Saur, J., Bunce, E. J., et al. (2018). Precipitating
777 Electron Energy Flux and Characteristic Energies in Jupiter's Main Auroral Region as Measured
778 by Juno/JEDI. *Journal of Geophysical Research: Space Physics*, 123(9), 7554–7567.
779 https://doi.org/10.1029/2018JA025639

780 Connerney, J. E. P., Acuña, M. H., & Ness, N. F. (1981). Modeling the Jovian current sheet and
781 inner magnetosphere. *Journal of Geophysical Research: Space Physics*, 86(A10), 8370–8384.
782 https://doi.org/10.1029/JA086iA10p08370

783 Connerney, J. E. P., Benn, M., Bjarno, J. B., Denver, T., Espley, J., Jorgensen, J. L., et al. (2017).
784 The Juno Magnetic Field Investigation. *Space Science Reviews*, 213(1), 39–138.
785 https://doi.org/10.1007/s11214-017-0334-z

786 Connerney, J. E. P., Kotsiaros, S., Oliversen, R. J., Espley, J. R., Joergensen, J. L., Joergensen, P.
787 S., et al. (2018). A New Model of Jupiter's Magnetic Field From Juno's First Nine
788 Orbits. *Geophysical Research Letters*, 45(6), 2590–2596. https://doi.org/10.1002/2018GL077312

789 Cowley, S. W. H., & Bunce, E. J. (2001). Origin of the main auroral oval in Jupiter's coupled
790 magnetosphere–ionosphere system. *Planetary and Space Science*, 49(10–11), 1067–1088.
791 https://doi.org/10.1016/S0032-0633(00)00167-7

792 Delamere, P. A., & Bagenal, F. (2010). Solar wind interaction with Jupiter's
793 magnetosphere. *Journal of Geophysical Research: Space Physics*, 115(A10).
794 https://doi.org/10.1029/2010JA015347

795 Ebert, R. W., Allegrini, F., Bagenal, F., Bolton, S. J., Connerney, J. E. P., Clark, G., et al. (2017).
796 Spatial Distribution and Properties of 0.1–100 keV Electrons in Jupiter's Polar Auroral
797 Region. *Geophysical Research Letters*, 44(18), 9199–9207.
798 https://doi.org/https://doi.org/10.1002/2017GL075106

Ebert, R. W., Greathouse, T. K., Clark, G., Hue, V., Allegrini, F., Bagenal, F., et al. (n.d.). Simultaneous UV Images and High-latitude Particle and Field Measurements During an Auroral Dawn Storm at Jupiter. *Journal of Geophysical Research: Space Physics*, e2021JA029679. https://doi.org/10.1029/2021JA029679

Elliott, S. S., Gurnett, D. A., Kurth, W. S., Clark, G., Mauk, B. H., Bolton, S. J., et al. (2018a). Pitch Angle Scattering of Upgoing Electron Beams in Jupiter's Polar Regions by Whistler Mode Waves. *Geophysical Research Letters*, 45(3), 1246–1252. https://doi.org/https://doi.org/10.1002/2017GL076878

Elliott, S. S., Gurnett, D. A., Kurth, W. S., Mauk, B. H., Ebert, R. W., Clark, G., et al. (2018b). The Acceleration of Electrons to High Energies Over the Jovian Polar Cap via Whistler Mode Wave-Particle Interactions. *Journal of Geophysical Research: Space Physics*, 123(9), 7523–7533. https://doi.org/https://doi.org/10.1029/2018JA025797

Elliott, S. S., Gurnett, D. A., Yoon, P. H., Kurth, W. S., Mauk, B. H., Ebert, R. W., et al. (2020). The Generation of Upward-Propagating Whistler Mode Waves by Electron Beams in the Jovian Polar Regions. *Journal of Geophysical Research: Space Physics*, 125(6), e2020JA027868. https://doi.org/https://doi.org/10.1029/2020JA027868

Elliott, S. S., Sulaiman, A. H., Kurth, W. S., Faden, J., Allegrini, F., Valek, P., et al. (2021). The High-Latitude Extension of Jupiter's Io Torus: Electron Densities Measured by Juno Waves. *Journal of Geophysical Research: Space Physics*, 126(8), e2021JA029195. https://doi.org/10.1029/2021JA029195

Ergun, R. E., Andersson, L., Main, D. S., Su, Y.-J., Carlson, C. W., McFadden, J. P., & Mozer, F. S. (2002). Parallel electric fields in the upward current region of the aurora: Indirect and direct observations. *Physics of Plasmas*, 9(9), 3685–3694. https://doi.org/10.1063/1.1499120

Ergun, R. E., Carlson, C. W., McFadden, J. P., Mozer, F. S., Delory, G. T., Peria, W., et al. (1998a). FAST satellite observations of electric field structures in the auroral zone. *Geophysical Research Letters*, 25(12), 2025–2028. https://doi.org/10.1029/98GL00635

Ergun, R. E., Carlson, C. W., McFadden, J. P., Mozer, F. S., Delory, G. T., Peria, W., et al. (1998b). FAST satellite observations of large-amplitude solitary structures. *Geophysical Research Letters*, 25(12), 2041–2044. https://doi.org/10.1029/98GL00636

Farrell, W. M., Gurnett, D. A., & Goertz, C. K. (1989). Coherent Cerenkov radiation from the Spacelab 2 electron beam. *Journal of Geophysical Research: Space Physics*, 94(A1), 443–452. https://doi.org/10.1029/JA094iA01p00443

Gershman, D. J., Connerney, J. E. P., Kotsiaros, S., DiBraccio, G. A., Martos, Y. M., F. -Viñas, A., et al. (2019). Alfvénic Fluctuations Associated With Jupiter's Auroral Emissions. *Geophysical Research Letters*, 46(13), 7157–7165. https://doi.org/https://doi.org/10.1029/2019GL082951

Gladstone, G. R., Persyn, S. C., Eterno, J. S., Walther, B. C., Slater, D. C., Davis, M. W., et al. (2017). The Ultraviolet Spectrograph on NASA's Juno Mission. *Space Science Reviews*, 213(1), 447–473. https://doi.org/10.1007/s11214-014-0040-z

838 Gladstone, G. R., Versteeg, M. H., Greathouse, T. K., Hue, V., Davis, M. W., Gérard, J.-C., et al.
839 (2017). Juno-UVS approach observations of Jupiter's auroras. *Geophysical Research*
840 *Letters*, 44(15), 7668–7675. https://doi.org/10.1002/2017GL073377

841 Gladstone, G. R., Waite, J. H., Grodent, D., Lewis, W. S., Crary, F. J., Elsner, R. F., et al. (2002).
842 A pulsating auroral X-ray hot spot on Jupiter. *Nature*, 415(6875), 1000–1003.
843 https://doi.org/10.1038/4151000a

844 Grodent, D. (2015). A Brief Review of Ultraviolet Auroral Emissions on Giant Planets. *Space*
845 *Science Reviews*, 187(1), 23–50. https://doi.org/10.1007/s11214-014-0052-8

846 Gurnett, D. A., & Shaw, R. R. (1973). Electromagnetic radiation trapped in the magnetosphere
847 above the plasma frequency. *Journal of Geophysical Research* (1896-1977), 78(34), 8136–8149.
848 https://doi.org/10.1029/JA078i034p08136

849 Gurnett, D. A. (1966). A satellite study of VLF hiss. *Journal of Geophysical Research* (1896-
850 1977), 71(23), 5599–5615. https://doi.org/10.1029/JZ071i023p05599

851 Gurnett, D. A., et al. (1983), Auroral hiss, Z mode radiation, and auroral kilometric radiation in
852 the polar magnetosphere: DE 1 observations, *Journal of Geophysical Research*, 88,
853 doi:10.1029/JA088iA01p00329

854 Gurnett, D. A., et al. (2011), Auroral hiss, electron beams and standing Alfvén wave currents near
855 Saturn's moon Enceladus, *Geophysical Research Letters*, 38, doi:10.1029/2011GL046854

856 Gurnett, D. A., Huff, R. L., Menietti, J. D., Burch, J. L., Winningham, J. D., & Shawhan, S. D.
857 (1984). Correlated low-frequency electric and magnetic noise along the auroral field
858 lines. *Journal of Geophysical Research: Space Physics*, 89(A10), 8971–8985.
859 https://doi.org/10.1029/JA089iA10p08971

860 Hill, T. W. (2001). The Jovian auroral oval. *Journal of Geophysical Research: Space*
861 *Physics*, 106(A5), 8101–8107. https://doi.org/10.1029/2000JA000302

862 Hill, T. W. (1979). Inertial limit on corotation. *Journal of Geophysical Research: Space*
863 *Physics*, 84(A11), 6554–6558. https://doi.org/10.1029/JA084iA11p06554

864 Hull, A. J., Bonnell, J. W., Mozer, F. S., & Scudder, J. D. (2003). A statistical study of large-
865 amplitude parallel electric fields in the upward current region of the auroral acceleration
866 region. *Journal of Geophysical Research: Space Physics*, 108(A1), SMP 5-1-SMP 5-23.
867 https://doi.org/10.1029/2001JA007540

868 Imai, M., Greathouse, T. K., Kurth, W. S., Gladstone, G. R., Louis, C. K., Zarka, P., et al.
869 (2019). Probing Jovian Broadband Kilometric Radio Sources Tied to the Ultraviolet Main
870 Auroral Oval With Juno. *Geophysical Research Letters*, 46(2), 571–579.
871 https://doi.org/10.1029/2018GL081227

872 James, H. G. VLF saucers, *J. Geophys. Res.*, **81**, 4 (1976). doi:10.1029/JA081i004p00501

873 Joy, S. P., Kivelson, M. G., Walker, R. J., Khurana, K. K., Russell, C. T., & Ogino, T. (2002).
874 Probabilistic models of the Jovian magnetopause and bow shock locations. *Journal of*
875 *Geophysical Research: Space Physics*, 107(A10), SMP 17-1-SMP 17-17.
876 https://doi.org/https://doi.org/10.1029/2001JA009146

877 Khurana, K. K., Kivelson, M. G., Vasyliunas, V. M., Krupp, N., Woch, J., Lagg, A., et al.
878 (2004). The configuration of Jupiter's magnetosphere. In F. Bagenal, T. E. Dowling, & W. B.
879 McKinnon (Eds.), *Jupiter: The planet, satellites, and magnetosphere* (pp. 593-616). New York.
880 Cambridge Uni. Press.

881 Kivelson, M. G., & Southwood, D. J. (2005). Dynamical consequences of two modes of
882 centrifugal instability in Jupiter's outer magnetosphere. *Journal of Geophysical Research: Space*
883 *Physics*, 110(A12). https://doi.org/10.1029/2005JA011176

884 Knight, S. (1973). Parallel electric fields. *Planetary and Space Science*, 21(5), 741–750.
885 https://doi.org/10.1016/0032-0633(73)90093-7

886 Kolmašová, I., Imai, M., Santolík, O., Kurth, W. S., Hospodarsky, G. B., Gurnett, D. A., et al.
887 (2018). Discovery of rapid whistlers close to Jupiter implying lightning rates similar to those on
888 Earth. *Nature Astronomy*, 2(7), 544–548. https://doi.org/10.1038/s41550-018-0442-z

889 Kotsiaros, S., Connerney, J. E. P., Clark, G., Allegrini, F., Gladstone, G. R., Kurth, W. S., et al.
890 (2019). Birkeland currents in Jupiter's magnetosphere observed by the polar-orbiting Juno
891 spacecraft. *Nature Astronomy*, 3(10), 904–909. https://doi.org/10.1038/s41550-019-0819-7

892 Kurth, W. S., Hospodarsky, G. B., Kirchner, D. L., Mokrzycki, B. T., Averkamp, T. F., Robison,
893 W. T., et al. (2017b). The Juno Waves Investigation. *Space Science Reviews*, 213(1), 347–392.
894 https://doi.org/10.1007/s11214-017-0396-y

895 Kurth, W. S., Imai, M., Hospodarsky, G. B., Gurnett, D. A., Louarn, P., Valek, P., et al. (2017a).
896 A new view of Jupiter's auroral radio spectrum. *Geophysical Research Letters*, 44(14), 7114–
897 7121. https://doi.org/10.1002/2017GL072889

898 Kurth, W. S., Mauk, B. H., Elliott, S. S., Gurnett, D. A., Hospodarsky, G. B., Santolik, O., et al.
899 (2018). Whistler Mode Waves Associated With Broadband Auroral Electron Precipitation at
900 Jupiter. *Geophysical Research Letters*, 45(18), 9372–9379.
901 https://doi.org/10.1029/2018GL078566

902 Li, W., Thorne, R. M., Ma, Q., Zhang, X.-J., Gladstone, G. R., Hue, V., et al. (2017).
903 Understanding the Origin of Jupiter's Diffuse Aurora Using Juno's First Perijove
904 Observations. *Geophysical Research Letters*, 44(20), 10,162-10,170.
905 https://doi.org/10.1002/2017GL075545

906 Li, W., Ma, Q., Shen, X.-C., Zhang, X.-J., Mauk, B. H., Clark, G., et al. (2021). Quantification of
907 Diffuse Auroral Electron Precipitation Driven by Whistler Mode Waves at Jupiter. *Geophysical*
908 *Research Letters*, 48(19), e2021GL095457. https://doi.org/10.1029/2021GL095457

909 Louarn, P., Allegrini, F., McComas, D. J., Valek, P. W., Kurth, W. S., André, N., et al. (2017).
910 Generation of the Jovian hectometric radiation: First lessons from Juno: Juno Observations in a

911 HOM Radio Source. *Geophysical Research Letters*, 44(10), 4439–4446.
912 https://doi.org/10.1002/2017GL072923

913 Louis, C. K., Prangé, R., Lamy, L., Zarka, P., Imai, M., Kurth, W. S., & Connerney, J. E. P.
914 (2019). Jovian Auroral Radio Sources Detected In Situ by Juno/Waves: Comparisons With
915 Model Auroral Ovals and Simultaneous HST FUV Images. *Geophysical Research*
916 *Letters*, 46(21), 11606–11614. https://doi.org/10.1029/2019GL084799

917 Lysak, R. L. (1986). Ion Acceleration by Wave-Particle Interaction. In Ion Acceleration in the
918 Magnetosphere and Ionosphere (pp. 261–270). American Geophysical Union (AGU).
919 https://doi.org/10.1029/GM038p0261

920 Lysak, R. L. (1991). Feedback instability of the ionospheric resonant cavity. *Journal of*
921 *Geophysical Research: Space Physics*, 96(A2), 1553–1568. https://doi.org/10.1029/90JA02154

922 Lysak, R. L., Song, Y., Elliott, S., Kurth, W., Sulaiman, A. H., & Gershman, D. (2021). The Jovian
923 Ionospheric Alfvén Resonator and Auroral Particle Acceleration. *Journal of Geophysical*
924 *Research: Space Physics*, e2021JA029886. https://doi.org/10.1029/2021JA029886

925 Maggs, J. E., et al. (1989), Nonlinear evolution of the auroral electron beam, *Journal of*
926 *Geophysical Research*, 94, doi:10.1029/JA094iA04p03631

927 Masters, A. (2017). Model-Based Assessments of Magnetic Reconnection and Kelvin-Helmholtz
928 Instability at Jupiter's Magnetopause. *Journal of Geophysical Research: Space Physics*, 122(11),
929 11,154-11,174. https://doi.org/10.1002/2017JA024736

930 Masters, A. (2018). A More Viscous-Like Solar Wind Interaction With All the Giant
931 Planets. *Geophysical Research Letters*, 45(15), 7320–7329.
932 https://doi.org/10.1029/2018GL078416

933 Masters, A., Dunn, W. R., Stallard, T. S., Manners, H., & Stawarz, J. (2021). Magnetic
934 Reconnection Near the Planet as a Possible Driver of Jupiter's Mysterious Polar
935 Auroras. *Journal of Geophysical Research: Space Physics*, 126(8), e2021JA029544.
936 https://doi.org/10.1029/2021JA029544

937 Matsumoto, H., Kojima, H., Miyatake, T., Omura, Y., Okada, M., Nagano, I., & Tsutsui, M.
938 (1994). Electrostatic solitary waves (ESW) in the magnetotail: BEN wave forms observed by
939 GEOTAIL. *Geophysical Research Letters*, 21(25), 2915–2918.
940 https://doi.org/10.1029/94GL01284

941 Mauk, B. H., Clark, G., Gladstone, G. R., Kotsiaros, S., Adriani, A., Allegrini, F., et al. (2020).
942 Energetic Particles and Acceleration Regions Over Jupiter's Polar Cap and Main Aurora: A
943 Broad Overview. *Journal of Geophysical Research: Space Physics*, 125(3), e2019JA027699.
944 https://doi.org/https://doi.org/10.1029/2019JA027699

945 Mauk, B. H., Haggerty, D. K., Paranicas, C., Clark, G., Kollmann, P., Rymer, A. M., et al.
946 (2017a). Juno observations of energetic charged particles over Jupiter's polar regions: Analysis
947 of monodirectional and bidirectional electron beams. *Geophysical Research Letters*, 44(10),
948 4410–4418. https://doi.org/10.1002/2016GL072286

949 Mauk, B. H., Haggerty, D. K., Paranicas, C., Clark, G., Kollmann, P., Rymer, A. M., et al.
950 (2017b). Discrete and broadband electron acceleration in Jupiter's powerful
951 aurora. *Nature*, 549(7670), 66–69. https://doi.org/10.1038/nature23648

952 Mauk, B. H., Haggerty, D. K., Jaskulek, S. E., Schlemm, C. E., Brown, L. E., Cooper, S. A., et
953 al. (2017c). The Jupiter Energetic Particle Detector Instrument (JEDI) Investigation for the Juno
954 Mission. *Space Science Reviews*, 213(1), 289–346. https://doi.org/10.1007/s11214-013-0025-3

955 Mauk, B. H., Haggerty, D. K., Paranicas, C., Clark, G., Kollmann, P., Rymer, A. M., et al.
956 (2018). Diverse Electron and Ion Acceleration Characteristics Observed Over Jupiter's Main
957 Aurora. *Geophysical Research Letters*, 45(3), 1277–1285.
958 https://doi.org/10.1002/2017GL076901

959 McComas, D. J., Alexander, N., Allegrini, F., Bagenal, F., Beebe, C., Clark, G., et al. (2017).
960 The Jovian Auroral Distributions Experiment (JADE) on the Juno Mission to Jupiter. *Space*
961 *Science Reviews*, 213(1), 547–643. https://doi.org/10.1007/s11214-013-9990-9

962 McComas, D. J., & Bagenal, F. (2007). Jupiter: A fundamentally different magnetospheric
963 interaction with the solar wind. *Geophysical Research Letters*, 34(20), 421–5.
964 http://doi.org/10.1029/2007GL031078

965 McFadden, J. P., Carlson, C. W., Ergun, R. E., Chaston, C. C., Mozer, F. S., Temerin, M., et al.
966 (1998). Electron modulation and ion cyclotron waves observed by FAST. *Geophysical Research*
967 *Letters*, 25(12), 2045–2048. https://doi.org/10.1029/98GL00855

968 McIlwain, C. E. (1961), Coordinates for mapping the distribution of magnetically trapped
969 particles, *Journal of Geophysical Research*, 66, doi:10.1029/JZ066i011p03681

970 Mitchell, D. G., Kurth, W. S., Hospodarsky, G. B., Krupp, N., Saur, J., Mauk, B. H., et al.
971 (2009). Ion conics and electron beams associated with auroral processes on Saturn. *Journal of*
972 *Geophysical Research: Space Physics*, 114(A2). https://doi.org/10.1029/2008JA013621

973 Mura, A., Adriani, A., Altieri, F., Connerney, J. E. P., Bolton, S. J., Moriconi, M. L., et al.
974 (2017). Infrared observations of Jovian aurora from Juno's first orbits: Main oval and satellite
975 footprints. *Geophysical Research Letters*, 44(11), 5308–5316.
976 https://doi.org/10.1002/2017GL072954

977 Nichols, J. D., & Cowley, S. W. H. (2004). Magnetosphere-ionosphere coupling currents in
978 Jupiter's middle magnetosphere: effect of precipitation-induced enhancement of the ionospheric
979 Pedersen conductivity. *Annales Geophysicae*, 22(5), 1799–1827.
980 https://doi.org/https://doi.org/10.5194/angeo-22-1799-2004

981 Paranicas, C., Mauk, B. H., Haggerty, D. K., Clark, G., Kollmann, P., Rymer, A. M., et al.
982 (2018). Intervals of Intense Energetic Electron Beams Over Jupiter's Poles. *Journal of*
983 *Geophysical Research: Space Physics*, 123(3), 1989–1999.
984 https://doi.org/https://doi.org/10.1002/2017JA025106

Paschmann, G., Haaland, S., & Treumann, R. (2003). The Aurora as a Universal Phenomenon. In G. Paschmann, S. Haaland, & R. Treumann (Eds.), Auroral Plasma Physics (pp. 415–434). Dordrecht: Springer Netherlands. https://doi.org/10.1007/978-94-007-1086-3_9

Persoon, A. M., Gurnett, D. A., Peterson, W. K., Waite Jr., J. H., Burch, J. L., & Green, J. L. (1988). Electron density depletions in the nightside auroral zone. *Journal of Geophysical Research: Space Physics*, 93(A3), 1871–1895. https://doi.org/10.1029/JA093iA03p01871

Persoon, A. M., Kurth, W. S., Gurnett, D. A., Groene, J. B., Sulaiman, A. H., Wahlund, J.-E., et al. (2019). Electron Density Distributions in Saturn's Ionosphere. *Geophysical Research Letters*, 46(6), 3061–3068. https://doi.org/10.1029/2018GL078020

Ray, L. C., Ergun, R. E., Delamere, P. A., & Bagenal, F. (2010). Magnetosphere-ionosphere coupling at Jupiter: Effect of field-aligned potentials on angular momentum transport. *Journal of Geophysical Research: Space Physics*, 115(A9). https://doi.org/https://doi.org/10.1029/2010JA015423

Ray, L. C., Su, Y.-J., Ergun, R. E., Delamere, P. A., & Bagenal, F. (2009). Current-voltage relation of a centrifugally confined plasma. *Journal of Geophysical Research: Space Physics*, 114(A4). https://doi.org/10.1029/2008JA013969

Santolík, O., & Gurnett, D. A. (2002). Propagation of auroral hiss at high altitudes: Propagation of auroral hiss at high altitudes. *Geophysical Research Letters*, 29(10), 119-1-119–4. https://doi.org/10.1029/2001GL013666

Santolík, O., et al. (2016), Propagation of equatorial noise to low altitudes: Decoupling from the magnetosonic mode, *Geophysical Research Letters*, 43, 13, doi:10.1002/2016GL069582

Saur, J., Janser, S., Schreiner, A., Clark, G., Mauk, B. H., Kollmann, P., et al. (2018). Wave-Particle Interaction of Alfvén Waves in Jupiter's Magnetosphere: Auroral and Magnetospheric Particle Acceleration. *Journal of Geophysical Research: Space Physics*, 123(11), 9560–9573. https://doi.org/https://doi.org/10.1029/2018JA025948

Saur, J., Politano, H., Pouquet, A., & Matthaeus, W. H. (2002). Evidence for weak MHD turbulence in the middle magnetosphere of Jupiter. *Astronomy & Astrophysics*, 386(2), 699–708. https://doi.org/10.1051/0004-6361:20020305

Saur, J., Pouquet, A., & Matthaeus, W. H. (2003). An acceleration mechanism for the generation of the main auroral oval on Jupiter. *Geophysical Research Letters*, 30(5). https://doi.org/https://doi.org/10.1029/2002GL015761

Shi, C., Zhao, J., Sun, H., Huang, C., & Xie, H. (2020). Electromagnetic Emission Driven by Electron Beam Instability in the Jovian Polar Regions. *The Astrophysical Journal*, 902(2), 151. https://doi.org/10.3847/1538-4357/abb5a1

Song, Y., & Lysak, R. L. (2006). Displacement Current and the Generation of Parallel Electric Fields. *Physical Review Letters*, 96(14), 145002. https://doi.org/10.1103/PhysRevLett.96.145002

Sulaiman, A. H. et al. (2018), Enceladus auroral hiss emissions during Cassini's Grand Finale, *Geophys. Res. Lett.*, **45**, 15, doi:10.1029/2018GL078130

Sulaiman, A. H., Elliott, S. S., Kurth, W. S., Faden, J. B., Hospodarsky, G. B., & Menietti, J. D. (2021). Inferring Jovian Electron Densities Using Plasma Wave Spectra Obtained by the Juno/Waves Instrument. *Journal of Geophysical Research: Space Physics*, 126(8), e2021JA029263. https://doi.org/10.1029/2021JA029263

Sulaiman, A. H., Hospodarsky, G. B., Elliott, S. S., Kurth, W. S., Gurnett, D. A., Imai, M., et al. (2020). Wave-Particle Interactions Associated With Io's Auroral Footprint: Evidence of Alfvén, Ion Cyclotron, and Whistler Modes. *Geophysical Research Letters*, 47(22), e2020GL088432. https://doi.org/10.1029/2020GL088432

Szalay, J. R., Allegrini, F., Bagenal, F., Bolton, S. J., Clark, G., Connerney, J. E. P., et al. (2017). Plasma measurements in the Jovian polar region with Juno/JADE. *Geophysical Research Letters*, 86(A8), 8447–9. http://doi.org/10.1002/2017GL072837

Szalay, J. R., Allegrini, F., Bagenal, F., Bolton, S. J., Clark, G., Connerney, J. E. P., et al. (2021). Proton Outflow Associated With Jupiter's Auroral Processes. *Geophysical Research Letters*, 48(1). https://doi.org/10.1029/2020GL091627

Temerin, M., Cerny, K., Lotko, W., & Mozer, F. S. (1982). Observations of Double Layers and Solitary Waves in the Auroral Plasma. *Physical Review Letters*, 48(17), 1175–1179. https://doi.org/10.1103/PhysRevLett.48.1175

Thomas, N., Bagenal, F., Hill, T. W., & Wilson, J. K. (2004). The Io neutral clouds and plasma torus. In F. Bagenal, T. E. Dowling, & W. B. McKinnon (Eds.), *Jupiter: The planet, satellites, and magnetosphere* (pp. 593-616). New York. Cambridge Uni. Press.

Waite, J. H., Gladstone, G. R., Lewis, W. S., Goldstein, R., McComas, D. J., Riley, P., et al. (2001). An auroral flare at Jupiter. *Nature*, 410(6830), 787–789. https://doi.org/10.1038/35071018

Wu, C. S., & Lee, L. C. (1979). A theory of the terrestrial kilometric radiation. *The Astrophysical Journal*, 230, 621-626. https://doi.org/10.1086/157120

Zhang, B., Delamere, P. A., Yao, Z., Bonfond, B., Lin, D., Sorathia, K. A., et al. (n.d.). How Jupiter's unusual magnetospheric topology structures its aurora. *Science Advances*, 7(15), eabd1204. https://doi.org/10.1126/sciadv.abd1204